

Hemodynamic Deconvolution Demystified: Sparsity-Driven Regularization at Work

Eneko Uruñuela^{a,b,*}, Thomas A.W. Bolton^{c,d}, Dimitri Van De Ville^{c,e}, César Caballero-Gaudes^{a,*}

^a*Basque Center on Cognition, Brain and Language (BCBL), Donostia-San Sebastián, Spain.*

^b*University of the Basque Country (EHU/UPV), Donostia-San Sebastián, Spain.*

^c*Ecole Polytechnique Fédérale de Lausanne (EPFL), Lausanne, Switzerland.*

^d*Gamma Knife Center, Department of Clinical Neuroscience, Centre Hospitalier Universitaire Vaudois (CHUV), Lausanne, Switzerland*

^e*Faculty of Medicine, University of Geneva, Geneva, Switzerland*

Abstract

Deconvolution of the hemodynamic response is an important step to access short timescales of brain activity recorded by functional magnetic resonance imaging (fMRI). Albeit conventional deconvolution algorithms have been around for a long time (e.g., Wiener deconvolution), recent state-of-the-art methods based on sparsity-pursuing regularization are attracting increasing interest to investigate brain dynamics and connectivity with fMRI. This technical note revisits the main concepts underlying two main methods, Paradigm Free Mapping and Total Activation, in the most accessible way. Despite their apparent differences in the formulation, these methods are theoretically equivalent as they represent the synthesis and analysis sides of the same problem, respectively. We demonstrate this equivalence in practice with their best-available implementations using both simulations, with different signal-to-noise ratios, and experimental fMRI data acquired during a motor task and resting-state. We evaluate the parameter settings that lead to equivalent results, and showcase the potential of these algorithms compared to other common approaches. This note is useful for practitioners interested in gaining a better understanding of state-of-the-art hemodynamic deconvolution, and aims to answer questions that practitioners often have regarding the differences between the two methods.

Keywords: fMRI deconvolution, paradigm free mapping, total activation, temporal regularization

1. Introduction

Functional magnetic resonance imaging (fMRI) data analysis is often directed to identify and disentangle the neural processes that occur in different brain regions during task or at rest. As the blood oxygenation level-dependent (BOLD) signal of fMRI is only a proxy for neuronal activity mediated through neurovascular coupling, an intermediate step that estimates the activity-inducing signal, at the timescale of fMRI, from the BOLD timeseries can be useful. Conventional analysis of task fMRI data relies on the general linear models (GLM) to establish statistical parametric maps of brain activity by regression of the empirical timecourses against hypothetical ones built from

*Corresponding authors

Email addresses: e.urunuela@bcbl.eu (Eneko Uruñuela), c.caballero@bcbl.eu (César Caballero-Gaudes)

9 the knowledge of the experimental paradigm. However, timing information of the paradigm can be
10 unknown, inaccurate, or insufficient in some scenarios such as naturalistic stimuli, resting-state, or
11 clinically-relevant assessments.

12 Deconvolution and methods alike are aiming to estimate neuronal activity by undoing the
13 blurring effect of the hemodynamic response, characterized as a hemodynamic response function
14 (HRF)¹. Given the inherently ill-posed nature of hemodynamic deconvolution, due to the strong
15 temporal low-pass characteristics of the HRF, the key is to introduce additional constraints in
16 the estimation problem that are typically expressed as regularizers. For instance, the so-called
17 Wiener deconvolution is expressing a “minimal energy” constraint on the deconvolved signal, and
18 has been used in the framework of psychophysiological interaction analysis to compute the interac-
19 tion between a seed’s activity-inducing timecourse and an experimental modulation (Glover, 1999;
20 Gitelman et al., 2003; Gerchen et al., 2014; Di and Biswal, 2018; Freitas et al., 2020). Complement-
21 arily, the interest in deconvolution has increased to explore time-varying activity in resting-state
22 fMRI data (Prete et al., 2017; Keilholz et al., 2017; Lurie et al., 2020; ?). In that case, the aim is
23 to gain better insights of the neural signals that drive functional connectivity at short time scales,
24 as well as learning about the spatio-temporal structure of functional components that dynamically
25 construct resting-state networks and their interactions (Karahanoğlu and Ville, 2017).

26 Deconvolution of the resting-state fMRI signal has illustrated the significance of transient, sparse
27 spontaneous events (Petridou et al., 2012; Allan et al., 2015) that refine the hierarchical clusteriza-
28 tion of functional networks (Karahanoğlu et al., 2013) and reveal their temporal overlap based
29 on their signal innovations not only in the human brain (Karahanoğlu and Ville, 2015), but also
30 in the spinal cord (Kinany et al., 2020). Similar to task-related studies, deconvolution allows to
31 investigate modulatory interactions within and between resting-state functional networks (Di and
32 Biswal, 2013, 2015). In addition, decoding of the deconvolved spontaneous events allows to decipher
33 the flow of spontaneous thoughts and actions across different cognitive and sensory domains while
34 at rest (Karahanoğlu and Ville, 2015; Gonzalez-Castillo et al., 2019; Tan et al., 2017). Beyond find-
35 ings on healthy subjects, deconvolution techniques have also proven its utility in clinical conditions
36 to characterize functional alterations of patients with a progressive stage of multiple sclerosis at
37 rest (Bommarito et al., 2020), to find functional signatures of prodromal psychotic symptoms and
38 anxiety at rest on patients suffering from schizophrenia (Zöller et al., 2019), to detect the foci of
39 interictal events in epilepsy patients without an EEG recording (Lopes et al., 2012; Karahanoglu
40 et al., 2013), or to study functional dissociations observed during non-rapid eye movement sleep
41 that are associated with reduced consolidation of information and impaired consciousness (Tarun
42 et al., 2020).

43 The algorithms for hemodynamic deconvolution can be classified based on the assumed hemo-
44 dynamic model and the optimization problem used to estimate the neuronal-related signal. Most
45 approaches assume a linear time-invariant model for the hemodynamic response that is inverted
46 by means of variational (regularized) least squares estimators (Glover, 1999; Gitelman et al., 2003;
47 Gaudes et al., 2010, 2012, 2013; Caballero-Gaudes et al., 2019; Hernandez-Garcia and Ulfarsson,
48 2011; Karahanoglu et al., 2013; Cherkaooui et al., 2019; Costantini et al., 2021; Hütel et al., 2021),
49 logistic functions (Bush and Cisler, 2013; Bush et al., 2015; Loula et al., 2018), probabilistic mixture
50 models (Pidnebesna et al., 2019), convolutional autoencoders (Hütel et al., 2018) or nonparamet-

¹Note that the term deconvolution is also alternatively employed to refer to the estimation of the hemodynamic response shape assuming a known activity-inducing signal or neuronal activity (Goutte et al., 2000; Marrelec et al., 2002; Ciuciu et al., 2003; Casanova et al., 2008).

ric homomorphic filtering (Sreenivasan et al., 2015). Alternatively, several methods have also been proposed to invert non-linear models of the neuronal and hemodynamic coupling (Riera et al., 2004; Penny et al., 2005; Friston et al., 2008; Havlicek et al., 2011; Aslan et al., 2016; Madi and Karameh, 2017; Ruiz-Euler et al., 2018).

Among the variety of approaches, those based on regularized least squares estimators have been employed more often due to their appropriate performance at small spatial scales (e.g., voxelwise). Relevant for this work, two different formulations can be established for the regularized least-squares deconvolution problem, either based on a synthesis- or analysis-based model (Elad et al., 2007; Ortelli and van de Geer, 2019). The rationale of the synthesis-based model is that we know or suspect that the true signal (here, the neuronally-driven BOLD component of the fMRI signal) can be represented as a linear combination of predefined patterns or dictionary atoms (for instance, the hemodynamic response function). In contrast, the analysis-based approach considers that the true signal is analyzed by some relevant operator and the resulting signal is small (i.e., sparse).

As members of the groups that developed Paradigm Free Mapping (synthesis-based solved with regularized least-squares estimators such as ridge-regression Gaudes et al. 2010 or LASSO Gaudes et al. 2013) and Total Activation (analysis-based also solved with a regularized least-squares estimator using generalized total variation Karahanoglu et al. 2011; Karahanoglu et al. 2013) deconvolution methods for fMRI data analysis, we are often contacted by researchers who want to know about the similarities and differences between the two methods and which one is better. It depends—and to clarify this point, this note revisits synthesis- and analysis-based deconvolution methods for fMRI data and comprises four sections. First, we present the theory behind these two deconvolution approaches based on regularized least squares estimators that promote sparsity: Paradigm Free Mapping (PFM) (Gaudes et al., 2013) — available in AFNI as 3dPFM² and 3dMEPFM³ for single-echo and multi-echo data, respectively — and Total Activation (TA) (Karahanoglu et al., 2013) — available as part of the iCAPs toolbox⁴. We describe the similarities and differences in their analytical formulations, and how they can be related to each other. Next, we assess their performance controlling for a fair comparison on simulated and experimental data. Finally, we discuss their benefits and shortcomings and conclude with our vision on potential extensions and developments.

2. Theory

2.1. Notations and definitions

Matrices of size N rows and M columns are denoted by boldface capital letters, e.g., $\mathbf{X} \in \mathbb{R}^{N \times M}$, whereas column vectors of length N are denoted as boldface lowercase letters, e.g., $\mathbf{x} \in \mathbb{R}^N$. Scalars are denoted by lowercase letters, e.g., k . Continuous functions are denoted by brackets, e.g., $h(t)$, while discrete functions are denoted by square brackets, e.g., $x[k]$. The Euclidean norm of a matrix \mathbf{X} is denoted as $\|\mathbf{X}\|_2$, the ℓ_1 -norm is denoted by $\|\mathbf{X}\|_1$ and the Frobenius norm is denoted by $\|\mathbf{X}\|_F$. The discrete integration (\mathbf{L}) and difference (\mathbf{D}) operators are defined as:

²https://afni.nimh.nih.gov/pub/dist/doc/program_help/3dPFM.html

³https://afni.nimh.nih.gov/pub/dist/doc/program_help/3dMEPFM.html

⁴<https://c4science.ch/source/iCAPs/>

$$\mathbf{L} = \begin{bmatrix} 1 & 0 & \dots & & \\ 1 & 1 & 0 & \dots & \\ 1 & 1 & 1 & 0 & \dots \\ \vdots & \ddots & \ddots & \ddots & \ddots \end{bmatrix}, \quad \mathbf{D} = \begin{bmatrix} 1 & 0 & \dots & & \\ 1 & -1 & 0 & \dots & \\ 0 & \ddots & \ddots & \ddots & \dots \\ \vdots & \ddots & 0 & 1 & -1 \end{bmatrix}.$$

88 *2.2. Conventional general linear model analysis*

Conventional general linear model (GLM) analysis puts forward a number of regressors incorporating the knowledge about the paradigm or behavior. For instance, the timing of epochs for a certain condition can be modeled as an indicator function $p(t)$ (e.g., Dirac functions for event-related designs or box-car functions for block-designs) convolved with the hemodynamic response function (HRF) $h(t)$, and sampled at TR resolution (Friston et al., 1994, 1998; Boynton et al., 1996; Cohen, 1997):

$$x(t) = p * h(t) \rightarrow x[k] = p * h(k \cdot \text{TR}).$$

The vector $\mathbf{x} = [x[k]]_{k=1,\dots,N} \in \mathbb{R}^N$ then constitutes the regressor modelling the hypothetical response, and several of them can be stacked as columns of the design matrix $\mathbf{X} = [\mathbf{x}_1 \dots \mathbf{x}_L] \in \mathbb{R}^{N \times L}$, leading to the well-known GLM formulation:

$$\mathbf{y} = \mathbf{X}\boldsymbol{\beta} + \mathbf{e}, \quad (1)$$

89 where the empirical timecourse $\mathbf{y} \in \mathbb{R}^N$ is explained by a linear combination of the regressors in \mathbf{X}
90 weighted by the parameters in $\boldsymbol{\beta} \in \mathbb{R}^L$ and corrupted by additive noise $\mathbf{e} \in \mathbb{R}^N$. Under independent
91 and identically distributed Gaussian assumptions of the latter, the maximum likelihood estimate of
92 the parameter weights reverts to the ordinary least-squares estimator; i.e., minimizing the residual
93 sum of squares between the fitted model and measurements. The number of regressors L is typically
94 much less than the number of measurements N , and thus the regression problem is over-determined
95 and does not require additional constraints or assumptions (Henson and Friston, 2007).

In the deconvolution approach, no prior knowledge of the hypothetical response is taken into account, and the purpose is to estimate the deconvolved activity-inducing signal \mathbf{s} from the measurements \mathbf{y} , which can be formulated as the signal model

$$\mathbf{y} = \mathbf{H}\mathbf{s} + \mathbf{e}, \quad (2)$$

where $\mathbf{H} \in \mathbb{R}^{N \times N}$ is a Toeplitz matrix that represents the discrete convolution with the HRF, and $\mathbf{s} \in \mathbb{R}^N$ is a length- N vector with the unknown activity-inducing signal. Note that the temporal resolution of the activity-inducing signal and the corresponding Toeplitz matrix is generally assumed to be equal to the TR of the acquisition, but it could also be higher if an upsampled estimate is desired. Despite the apparent similarity with the GLM equation, there are two important differences. First, the multiplication with the design matrix of the GLM is an expansion as a weighted linear combination of its columns, while the multiplication with the HRF matrix represents a convolution operator. Second, determining \mathbf{s} is an ill-posed problem given the nature of the HRF. As it can be seen intuitively, the convolution matrix \mathbf{H} is highly collinear (i.e., its columns are highly correlated) due to large overlap between shifted HRFs (see Figure 2C), thus introducing uncertainty in the estimates of \mathbf{s} when noise is present. Consequently, additional assumptions under the form of

regularization terms (or priors) in the estimate are needed to reduce their variance. In the least squares sense, the optimization problem to solve is given by

$$\hat{\mathbf{s}} = \arg \min_{\mathbf{s}} \frac{1}{2} \|\mathbf{y} - \mathbf{H}\mathbf{s}\|_2^2 + \Omega(\mathbf{s}). \quad (3)$$

The first term quantifies data fitness, which can be justified as the log-likelihood term derived from Gaussian noise assumptions, while the second term $\Omega(\mathbf{s})$ brings in regularization and can be interpreted as a prior on the activity-inducing signal. For example, the ℓ_2 -norm of \mathbf{s} (i.e., $\Omega(\mathbf{s}) = \lambda \|\mathbf{s}\|_2^2$) is imposed for ridge regression or Wiener deconvolution, which introduces a trade-off between the data fit term and “energy” of the estimates that is controlled by the regularization parameter λ . regularized terms are related to the elastic net (i.e., $\Omega(\mathbf{x}) = \lambda_1 \|\mathbf{x}\|_2^2 + \lambda_2 \|\mathbf{x}\|_1$) [REF].

2.3. Paradigm Free Mapping

In paradigm free mapping (PFM), the formulation of Eq. (3) was considered equivalently as fitting the measurements using the atoms of the HRF dictionary (i.e., columns of \mathbf{H}) with corresponding weights (entries of \mathbf{s}). This model corresponds to a synthesis formulation. In Gaudes et al. 2013 a sparsity-pursuing regularization term was introduced on \mathbf{s} , which in a strict way reverts to choosing $\Omega(\mathbf{s}) = \lambda \|\mathbf{s}\|_0$ as the regularization term and solving the optimization problem (Bruckstein et al., 2009). However, finding the optimal solution to the problem demands an exhaustive search across all possible combinations of the columns of \mathbf{H} . Hence, a pragmatic solution is to solve the convex-relaxed optimization problem for the ℓ_1 -norm, commonly known as Basis Pursuit Denoising (Chen et al., 2001) or equivalently as the least absolute shrinkage and selection operator (LASSO) (Tibshirani, 1996):

$$\hat{\mathbf{s}} = \arg \min_{\mathbf{s}} \frac{1}{2} \|\mathbf{y} - \mathbf{H}\mathbf{s}\|_2^2 + \lambda \|\mathbf{s}\|_1, \quad (4)$$

which provides fast convergence to a global solution. Imposing sparsity on the activity-inducing signal implies that it is assumed to be well represented by a reduced subset of few non-zero coefficients at the fMRI timescale, which in turn trigger event-related BOLD responses. Hereinafter, we refer to this assumption as the *spike model*. [However, even if PFM was developed as a spike model, its formulation in Eq.\(4\) can be extended to estimate the innovation signal, i.e., the derivative of the activity-inducing signal, as shown in section 2.5.](#)

2.4. Total Activation

Alternatively, deconvolution can be formulated as if the signal to be recovered directly fits the measurements and at the same time satisfies some suitable regularization, which leads to

$$\hat{\mathbf{x}} = \arg \min_{\mathbf{x}} \frac{1}{2} \|\mathbf{y} - \mathbf{x}\|_2^2 + \Omega(\mathbf{x}). \quad (5)$$

Under this analysis formulation, total variation (TV), i.e., the ℓ_1 -norm of the derivative $\Omega(\mathbf{x}) = \lambda \|\mathbf{D}\mathbf{x}\|_1$, is a powerful regularizer since it favors recovery of piecewise-constant signals (Chambolle, 2004). Going beyond, the approach of generalized TV introduces an additional differential operator $\mathbf{D}_{\mathbf{H}}$ in the regularizer that can be tailored as the inverse operator of a linear system (Karahanoglu et al., 2011), that is, $\Omega(\mathbf{x}) = \lambda \|\mathbf{D}\mathbf{D}_{\mathbf{H}}\mathbf{x}\|_1$. In the context of hemodynamic deconvolution, Total Activation is proposed for which the discrete operator $\mathbf{D}_{\mathbf{H}}$ is derived from the inverse of the continuous-domain linearized Balloon-Windkessel model (Buxton et al., 1998; Friston et al., 2000).

¹¹⁷ The interested reader is referred to (Khalidov et al., 2011; Karahanoglu et al., 2011; Karahanoglu
¹¹⁸ et al., 2013) for a detailed description of this derivation.

Therefore, the solution of the Total Activation (TA) problem

$$\hat{\mathbf{x}} = \arg \min_{\mathbf{x}} \frac{1}{2} \|\mathbf{y} - \mathbf{x}\|_2^2 + \lambda \|\mathbf{D}\mathbf{D}_{\mathbf{H}}\mathbf{x}\|_1 \quad (6)$$

¹¹⁹ will yield the activity-related signal \mathbf{x} for which the activity-inducing signal $\mathbf{s} = \mathbf{D}_{\mathbf{H}}\mathbf{x}$ and the
¹²⁰ so-called innovation signal $\mathbf{u} = \mathbf{D}\mathbf{s}$, i.e., the derivate of the activity-inducing signal, will also be
¹²¹ available, as they are required for the regularization. We refer to modeling the activity-inducing
¹²² signal based on the innovation signal as the *block model*. Nevertheless, even if TA was originally
¹²³ developed as a block model, its formulation in Eq.(6) can be made equivalent to the spike model
¹²⁴ as shown in section 2.5.

¹²⁵ 2.5. Unifying both perspectives

¹²⁶ PFM and TA are based on the synthesis- and analysis-based formulation of the deconvolution
¹²⁷ problem, respectively. They are also tailored for the spike and block model, respectively. In the first
¹²⁸ case, the recovered deconvolved signal is synthesized to be matched to the measurements, while in
¹²⁹ the second case, the recovered signal is directly matched to the measurements but needs to satisfy
¹³⁰ its analysis in terms of deconvolution. This also corresponds to using the forward or backward
¹³¹ model of the hemodynamic system, respectively. Hence, it is possible to make both approaches
¹³² equivalent (Elad et al., 2007)⁵.

¹³³ To start with, TA can be made equivalent to PFM by adapting it for the spike model; i.e., when
¹³⁴ removing the derivative operator \mathbf{D} of the regularizer in Eq. (6), it can be readily verified that
¹³⁵ replacing in that case $\mathbf{x} = \mathbf{H}\mathbf{s}$ leads to identical equations and thus both assume a spike model,
¹³⁶ since \mathbf{H} and $\mathbf{D}_{\mathbf{H}}$ will cancel out each other (Karahanoglu et al., 2011)⁶.

Conversely, the PFM spike model can also accommodate the TA block model by modifying Eq.
(4) with the forward model $\mathbf{y} = \mathbf{H}\mathbf{L}\mathbf{u} + \mathbf{e}$. Here, the activity-inducing signal \mathbf{s} is rewritten in terms
of the innovation signal \mathbf{u} as $\mathbf{s} = \mathbf{L}\mathbf{u}$ where the matrix \mathbf{L} is the first-order integration operator
(Cherkaoui et al., 2019; Uruñuela et al., 2020). This way, PFM can estimate the innovation signal
 \mathbf{u} as follows:

$$\hat{\mathbf{u}} = \arg \min_{\mathbf{u}} \frac{1}{2} \|\mathbf{y} - \mathbf{H}\mathbf{L}\mathbf{u}\|_2^2 + \lambda \|\mathbf{u}\|_1, \quad (7)$$

¹³⁷ and becomes equivalent to TA by replacing $\mathbf{u} = \mathbf{D}\mathbf{D}_{\mathbf{H}}\mathbf{x}$, and thus adopting the block model. Based
¹³⁸ on the previous equations (4), (6) and (7), it is clear that both PFM and TA can operate under the
¹³⁹ spike and block models, providing a convenient signal model according to the different assumptions
¹⁴⁰ of the underlying neuronal-related signal. This work evaluates the core of the two techniques; i.e.,
¹⁴¹ the regularized least-squares problem with temporal regularization without considering the spatial
¹⁴² regularization term originally incorporated in TA. For the remainder of this paper, we will use the
¹⁴³ PFM and TA formalisms with both spike and block models.

⁵Without dwelling into technicalities, for total variation, this equivalence is correct up to the constant, which is in the null space of the derivative operator.

⁶Again, this holds up to elements of the null space.

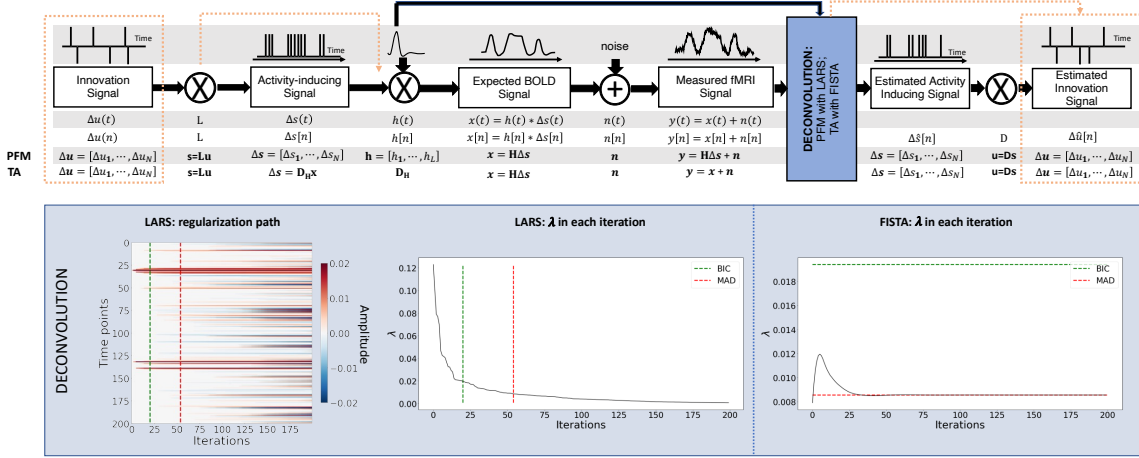


Figure 1: Flowchart detailing the different steps of the fMRI signal and the deconvolution methods described. The orange arrows indicate the flow to estimate the innovation signals, i.e., the derivative of the activity-inducing signal. The blue box depicts the iterative *modus operandi* of the two algorithms used in this paper to solve the paradigm free mapping (PFM) and total activation (TA) deconvolution problems. The plot on the left shows the regularization path obtained with the least angle regression (LARS) algorithm, where the x-axis illustrates the different iterations of the algorithm, the y-axis represents points in time, and the color describes the amplitude of the estimated signal. The middle plot depicts the decreasing values of λ for each iteration of LARS as the regularization path is computed. The green and red dashed lines in both plots illustrate the Bayesian information criterion (BIC) and median absolute deviation (MAD) solutions, respectively. Comparatively, the changes in λ when the fast iterative shrinkage-thresholding algorithm (FISTA) method is made to converge to the MAD estimate of the noise are shown on the right. Likewise, the λ corresponding to the BIC and MAD solutions are shown with dashed lines.

2.6. Algorithms and parameter selection

Despite their apparent resemblance, the practical implementations of the PFM and TA methods proposed different algorithms to solve the corresponding optimization problem and select an adequate regularization parameter λ (Gaudes et al., 2013; Karahanoglu et al., 2013). The PFM implementation available in AFNI employs the least angle regression (LARS) (Efron et al., 2004), whereas the TA implementation uses the fast iterative shrinkage-thresholding algorithm (FISTA) (Beck and Teboulle, 2009). The blue box in Figure 1 provides a descriptive view of the iterative *modus operandi* of the two algorithms.

On the one hand, LARS is a homotopy approach that computes all the possible solutions to the optimization problem and their corresponding value of λ ; i.e., the regularization path, and the solution according to the Bayesian Information Criterion (BIC) (Schwarz, 1978), was recommended as the most appropriate in the case of PFM approaches since AIC often tends to overfit the signal(Gaudes et al., 2013; Caballero-Gaudes et al., 2019).

On the other hand, FISTA is an extension of the classical gradient algorithm that provides fast convergence for large-scale problems. In the case of FISTA though, the regularization parameter λ must be selected prior to solving the problem, but can be updated in every iteration so that the residuals of the data fit converge to an estimated noise level of the data $\hat{\sigma}$:

$$\lambda^{n+1} = \frac{N\hat{\sigma}}{\frac{1}{2}\|\mathbf{y} - \mathbf{x}^n\|_F^2} \lambda^n, \quad (8)$$

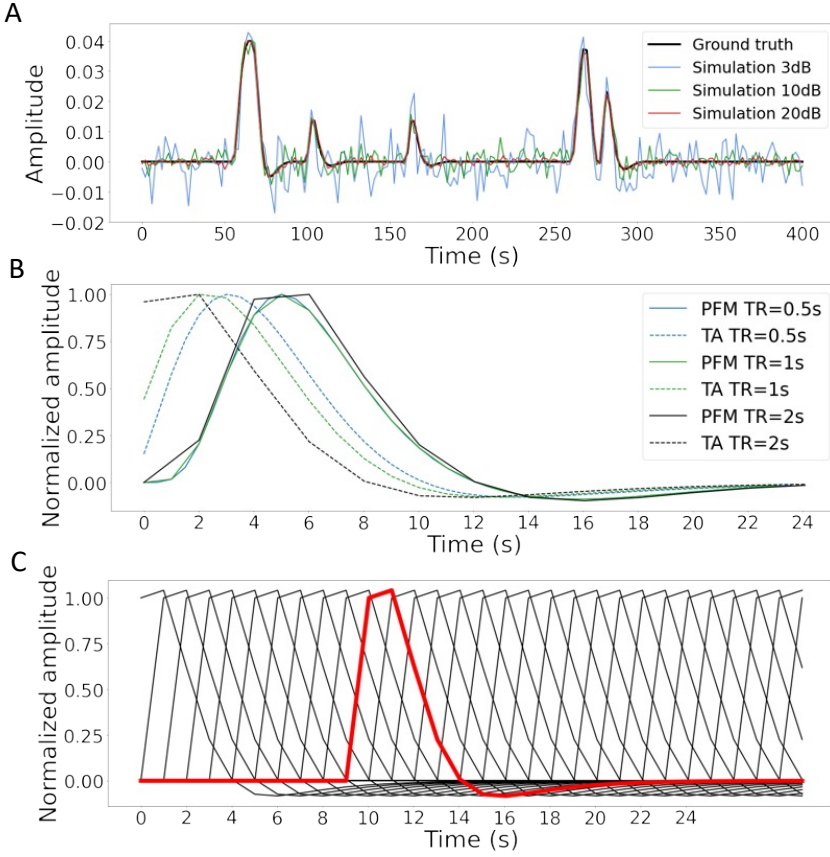


Figure 2: A) Simulated signal with different SNRs (20 dB, 10 dB and 3 dB) and ground truth given in signal percentage change (SPC). B) Canonical HRF models typically used by PFM (solid line) and TA (dashed line) at TR = 0.5 s (blue), TR = 1 s (green) and TR = 2 s (black). Without loss of generality, the waveforms are scaled to unit amplitude for visualization. C) Representation of shifted HRFs at TR = 2 s that build the design matrix for PFM when the HRF model has been matched to that in TA. The red line corresponds to one of the columns of the HRF matrix.

157 where x^n is the n^{th} iteration estimate, λ^n and λ^{n+1} are the n^{th} and $n + 1^{th}$ iteration values for the
 158 regularization parameter λ , and N is the number of points in the time-course. The pre-estimated
 159 noise level can be obtained as the median absolute deviation (MAD) of the fine-scale wavelet
 160 coefficients (Daubechies, order 3) of the fMRI timecourse. The MAD criterion has been adopted
 161 in TA (Karahanoglu et al., 2013). Of note, similar formulations based on the MAD estimate have
 162 also been applied in PFM formulations (Gaudes et al., 2012, 2011).

163 **3. Methods**

164 *3.1. Simulated data*

In order to compare the two methods while controlling for their correct performance, we created a simulation scenario that can be found in the GitHub repository shared in Section 6. For the sake of illustration, we describe here the simulations corresponding to a timecourse with a duration of 400 seconds ($TR = 2$ s) where the activity-inducing signal includes 5 events, which are convolved with the canonical HRF. Different noise sources (physiological, thermal, and motion-related) were also added and we simulated three different scenarios with varying signal-to-noise ratios (SNR = [20 dB, 10 dB, 3 dB]) that represent high, medium and low contrast-to-noise ratios as shown in Figure 2A. Noise was created following the procedure in (Gaudes et al., 2013) as the sum of uncorrelated Gaussian noise and sinusoidal signals to simulate a realistic noise model with thermal noise, cardiac and respiratory physiological fluctuations, respectively. The physiological signals were generated as

$$\sum_{i=1}^2 \frac{1}{2^{i-1}} (\sin(2\pi f_{r,i}t + \phi_{r,i}) + \sin(2\pi f_{c,i}t + \phi_{c,i})), \quad (9)$$

165 with up to second-order harmonics per cardiac ($f_{c,i}$) and respiratory ($f_{r,i}$) component that were
166 randomly generated following normal distributions with variance 0.04 and mean if_r and if_c , for
167 $i = [1, 2]$. We set the fundamental frequencies to $f_r = 0.3$ Hz for the respiratory component (Birn
168 et al., 2006)) and $f_c = 1.1$ Hz for the cardiac component (Shmueli et al., 2007)). The phases of
169 each harmonic ϕ were randomly selected from a uniform distribution between 0 and 2π radians.
170 To simulate physiological noise that is proportional to the change in BOLD signal, a variable ratio
171 between the physiological (σ_P) and the thermal (σ_0) noise was modeled as $\sigma_P/\sigma_0 = a(tSNR)^b + c$,
172 where $a = 5.01 \times 10^{-6}$, $b = 2.81$, and $c = 0.397$, following the experimental measures available in
173 Table 3 from (Triantafyllou et al., 2005)).

174 *3.2. Experimental data*

175 To compare the performance of the two approaches as well as illustrate their operation, we
176 employ two representative experimental datasets.

177 **Motor task dataset:** One healthy subject was scanned in a 3T MR scanner (Siemens) under a
178 Basque Center on Cognition, Brain and Language Review Board-approved protocol. T2*-weighted
179 multi-echo fMRI data was acquired with a simultaneous-multislice multi-echo gradient echo-planar
180 imaging sequence, kindly provided by the Center of Magnetic Resonance Research (University
181 of Minnesota, USA) (Feinberg et al., 2010; Moeller et al., 2010; Setsompop et al., 2011), with the
182 following parameters: 340 temporal frames, 52 slices, Partial-Fourier = 6/8, voxel size = $2.4 \times 2.4 \times 3$
183 mm³, TR = 1.5 s, TEs = 10.6/28.69/46.78/64.87/82.96 ms, flip angle = 70°, multiband factor =
184 4, GRAPPA = 2.

185 During the fMRI acquisition, the subject performed a motor task consisting of five different
186 movements (left-hand finger tapping, right-hand finger tapping, moving the left toes, moving the
187 right toes and moving the tongue) that were visually cued through a mirror located on the head
188 coil. These conditions were randomly intermixed every 16 seconds, and were only repeated once
189 the entire set of stimuli were presented. Data preprocessing consisted of first, discarding the first 10
190 volumes of the functional data to achieve a steady state of magnetization. Then, image realignment
191 to the skull-stripped single-band reference image (SBRef) was computed on the first echo, and the
192 estimated rigid-body spatial transformation was applied to all other echoes (Jenkinson et al., 2012;
193 Jenkinson and Smith, 2001). A brain mask obtained from the SBRef volume was applied to all the
194 echoes and the different echo timeseries were optimally combined (OC) voxelwise by weighting each

timeseries contribution by its T2* value (Posse et al., 1999). AFNI (Cox, 1996) was employed for a detrending of up to 4th-order Legendre polynomials, within-brain spatial smoothing (3 mm FWHM) and voxelwise signal normalization to percentage change. Finally, distortion field correction was performed on the OC volume with Topup (Andersson et al., 2003), using the pair of spin-echo EPI images with reversed phase encoding acquired before the ME-EPI acquisition (Glasser et al., 2016).

Resting-state datasets: One healthy subject was scanned in a 3T MR scanner (Siemens) under a Basque Center on Cognition, Brain and Language Review Board-approved protocol. Two runs of T2*-weighted fMRI data were acquired during resting-state, each with 10 min duration, with 1) a standard gradient-echo echo-planar imaging sequence (monoband) (TR = 2000 ms, TE = 29 ms, flip-angle = 78°, matrix size = 64 × 64, voxel size = 3 × 3 × 3 mm³, 33 axial slices with interleaved acquisition, slice gap = 0.6 mm) and 2) a simultaneous-multislice gradient-echo echo-planar imaging sequence (multiband factor = 3, TR = 800 ms, TE = 29 ms, flip-angle = 60°, matrix size = 64 × 64, voxel size = 3 × 3 × 3 mm³, 42 axial slices with interleaved acquisition, no slice gap). Single-band reference images were also collected in both resting-state acquisitions for head motion realignment. Field maps were also obtained to correct for field distortions.

During both acquisitions, participants were instructed to keep their eyes open, fixating a white cross that they saw through a mirror located on the head coil, and not to think about anything specific. The data was pre-processed using AFNI (Cox, 1996). First, volumes corresponding to the initial 10 seconds were removed to allow for a steady-state magnetization. Then, the voxel time-series were despiked to reduce large-amplitude deviations and slice-time corrected. Inhomogeneities caused by magnetic susceptibility were corrected with FUGUE (FSL) using the field map images (Jenkinson et al., 2012). Next, functional images were realigned to a base volume (monoband: volume with the lowest head motion; multiband: single-band reference image). Finally, a simultaneous nuisance regression step was performed comprising up to 6th-order Legendre polynomials, low-pass filtering with a cutoff frequency of 0.25 Hz (only on multiband data to match the frequency content of the monoband), 6 realignment parameters plus temporal derivatives, 5 principal components of white matter (WM), 5 principal components of lateral ventricle voxels (anatomical CompCor) (Behzadi et al., 2007) and 5 principal components of the brain's edge voxels ,(Patriat et al., 2015). WM, CSF and brain's edge-voxel masks were obtained from Freesurfer tissue and brain segmentations. In addition, scans with potential artifacts were identified and censored when the euclidean norm of the temporal derivative of the realignment parameters (ENORM) was larger than 0.4, and the proportion of voxels adjusted in the despiking step exceeded 10%.

3.3. Selection of the hemodynamic response function

In their original formulations, PFM and TA specify the discrete-time HRF in different ways. For PFM, the continuous-domain specification of the canonical double-gamma HRF (Henson and Friston, 2007) is sampled at the TR and then put as shifted impulse responses to build the matrix \mathbf{H} . In the case of TA, however, the continuous-domain linearized version of the balloon-windkessel model is discretized to build the linear differential operator in $\mathbf{D}_\mathbf{H}$. While the TR only changes the resolution of the HRF shape for PFM, the impact of an equivalent impulse response of the discretized differential operator at different TR is more pronounced. As shown in Figure 2B, longer TR leads to equivalent impulse responses of TA that are shifted in time, provoking a lack of the initial baseline and rise of the response. We refer the reader to Figure S1 to see the differences in the estimation of the activity-inducing and innovation signals when both methods use the HRF in their original formulation. To avoid differences between PFM and TA based on their built-in

239 HRF, we choose to build the synthesis operator \mathbf{H} with shifted versions of the HRF given by the
 240 TA analysis operator (e.g., see Figure 2C for the TR=2s case).

241 *3.4. Selection of the regularization parameter*

242 We use the simulated data to compare the performance of the two deconvolution algorithms
 243 with both BIC and MAD criteria to set the regularization parameter λ (see section 2.6). We also
 244 evaluate if the algorithms behave differently in terms of the estimation of the activity-inducing
 245 signal $\hat{\mathbf{s}}$ using the spike model described in (4) and the block model based on the innovation signal
 246 $\hat{\mathbf{u}}$ in (7).

247 For selection based on the BIC, LARS was initially performed with the PFM deconvolution
 248 model to obtain the solution for every possible λ in the regularization path. Then, the values of λ
 249 corresponding to the BIC optimum were adopted to solve the TA deconvolution model by means
 250 of FISTA.

251 For a selection based on the MAD estimate of the noise, we apply the temporal regularization in
 252 its original form for TA, whereas for PFM the selected λ corresponds to the solution whose residuals
 253 have the closest standard deviation to the estimated noise level of the data $\hat{\sigma}$.

254 *3.5. Analyses in experimental fMRI data*

Difference between approaches: To assess the discrepancies between both approaches when applied on experimental fMRI data, we calculate the square root of the sum of squares of the differences (RSSD) between the activity-inducing signals estimated with PFM and TA on the three experimental datasets as

$$\text{RSSD} = \sqrt{\frac{1}{N} \sum_{k=1}^N (\hat{s}_{\text{PFM}}[k] - \hat{s}_{\text{TA}}[k])^2}, \quad (10)$$

255 where N is the number of timepoints of the acquisition. The RSSD of the innovation signals $\hat{\mathbf{u}}$ was
 256 computed equally.

257 **Task fMRI data:** In the analysis of the motor task data, we evaluate the performance of PFM
 258 and TA in comparison with a conventional General Linear Model analysis (*3dDeconvolve* in AFNI)
 259 that takes advantage of the information about the duration and onsets of the motor trials. Given
 260 the block design of the motor task, we only make this comparison with the block model.

261 **Resting-state fMRI data:** We also illustrate the usefulness of deconvolution approaches in
 262 the analysis of resting-state data where information about the timings of neuronal-related BOLD
 263 activity cannot be predicted. Apart from being able to explore individual maps of deconvolved
 264 activity (i.e., innovation signals, activity-inducing signals, or hemodynamic signals) at the temporal
 265 resolution of the acquisition (or deconvolution), here we calculate the [average extreme points of the](#)
 266 [activity-inducing and innovation maps \(given that these examples do not have a sufficient number](#)
 267 [of scans to perform a clustering step\)](#) and illustrate how popular approaches like co-activation
 268 patterns (CAPs)(Tagliazucchi et al., 2012; Liu et al., 2018) and innovation-driven co-activation
 269 patterns (iCAPs) (Karahanoglu and Ville, 2015) can be applied on the deconvolved signals to reveal
 270 patterns of coordinated brain activity. To achieve this, we calculate the average time-series in a seed
 271 of 9 voxels located in the precuneus, supramarginal gyrus, and occipital gyri independently, and
 272 solve the deconvolution problem to find the activity-inducing and innovation signals in the seeds.
 273 We then apply a 95th percentile threshold and average the maps of the time-frames that survive the
 274 threshold. Finally, we apply the same procedure to the original— i.e., non-deconvolved— signal in
 275 the seed and compare the results with the widely-used seed correlation approach.

276 **4. Results**

277 *4.1. Performance based on the regularization parameter*

278 Figure 3A shows the regularization paths of PFM and TA side by side obtained for the spike
279 model of Eq. (4) for SNR=3 dB. The solutions for all three SNR conditions are shown in Figures S2
280 and S3. Starting from the maximum λ corresponding to a null estimate and for decreasing values
281 of λ , LARS computes a new estimate at the value of λ that reduces the sparsity promoted by the
282 l_1 -norm and causes a change in the active set of non-zero coefficients of the estimate (i.e., a zero
283 coefficient becomes non-zero or vice versa) as shown in the horizontal axis of the heatmaps. Vertical
284 dashed lines depict the selection of the regularization parameter based on the BIC, and thus, the
285 colored coefficients indicated by these depict the estimated activity-inducing signal \hat{s} . Figure 3B
286 illustrates the resulting estimates of the activity-inducing and activity-related hemodynamic signals
287 when basing the selection of λ on the BIC for SNR=3 dB. Given that the regularization paths of
288 both approaches are identical, it can be clearly observed that the BIC-based estimates are identical
289 too for the corresponding λ . Thus, Figures 3A, 3B, S2 and S3 demonstrate that, regardless of
290 the simulated SNR condition, the spike model of both deconvolution algorithms produces identical
291 regularization paths when the same HRF and regularization parameters are applied, and hence,
292 identical estimates of the activity-inducing signal \hat{s} and neuronal-related hemodynamic signal \hat{x} .
293 Likewise, Figure 3C demonstrates that the regularization paths for the block model defined in
294 Eqs. (6) and (7) also yield virtually identical estimates of the innovation signals for both PFM and
295 TA methods. Again, the BIC-based selection of λ is identical for both PFM and TA. As illustrated
296 in Figure 3D, the estimates of the innovation signal u also show no distinguishable differences
297 between the algorithms. Figures 3 A-D demonstrate that both PFM and TA yield equivalent
298 regularization paths and estimates of the innovation signal and activity-inducing signal regardless
299 of the simulated SNR condition when applying the same HRF and regularization parameters with
300 the block and spike models.

301 As for selecting λ with the MAD criterion defined in Eq. (8), Figure 3E depicts the estimated
302 activity-inducing and activity-related signals for the simulated low-SNR setting using the spike
303 model, while Figure 3F shows the estimated signals corresponding to the block model. Both plots
304 in Figure 3E and F depict nearly identical results between PFM and TA with both models. Given
305 that the regularization paths of both techniques are identical, minor dissimilarities are owing to the
306 slight differences in the selection of λ due to the quantization of the values returned by LARS.

307 *4.2. Performance on experimental data*

308 Figure 4 depicts the RSSD maps revealing differences between PFM and TA estimates for
309 the spike (Figure 4A and C) and block (Figure 4B and D) models when applied to the three
310 experimental fMRI datasets. The RSSD values are virtually negligible (i.e., depicted in yellow)
311 in most of the within-brain voxels and lower than the amplitude of the estimates of the activity-
312 inducing and innovation signals. Based on the maximum value of the range shown in each image,
313 we observe that the similarity between both approaches is more evident for the spike model (with
314 both selection criteria) and the block model with the BIC selection. However, given the different
315 approaches used for the selection of the regularization parameter λ based on the MAD estimate
316 of the noise (i.e., converging so that the residuals of FISTA are equal to the MAD estimate of the
317 noise for TA vs. finding the LARS residual that is closest to the MAD estimate of the noise),
318 higher RSSD values can be observed with the largest differences occurring in gray matter voxels.
319 These areas also correspond to low values of λ (see Figure S4) and MAD estimates of the noise

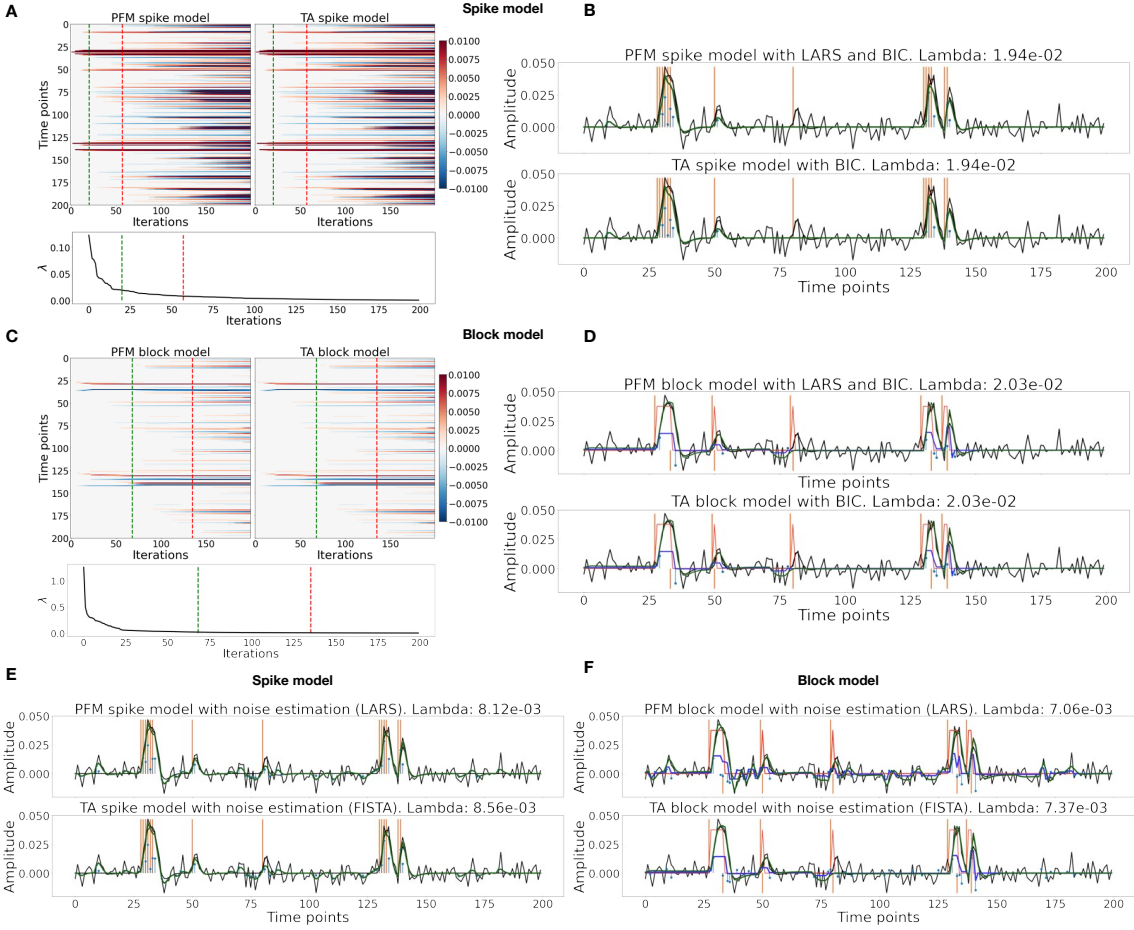


Figure 3: (A) Heatmap of the regularization paths of the activity-inducing signals (spike model) estimated with PFM and TA as a function of λ for the simulated data with SNR = 3 dB (x-axis: increasing number of iterations or λ as given by LARS; y-axis: time; color: amplitude). Vertical lines denote iterations corresponding to the BIC (dashed line) and MAD (dotted line) selection of λ . (B) Estimated activity-inducing (blue) and activity-related (green) signals with a selection of λ based on the BIC. Orange and red lines depict the ground truth. (C) Heatmap of the regularization paths of the innovation signals (block model) estimated with PFM and TA as a function of λ for the simulated data with SNR = 3 dB. (D) Estimated innovation (blue), activity-inducing (darker blue), and activity-related (green) signals with a selection of λ based on the BIC. (E) Activity-inducing and activity-related (fit, \times) signals estimated with PFM (top) and TA (bottom) when λ is selected based on the MAD method with the spike model, and (F) with the block model for the simulated data with SNR = 3 dB.

320 (see Figure S5), while the highest values are visible in regions with signal dropouts, ventricles,
 321 and white matter. These differences that arise from the differing methods to find the optimal
 322 regularization parameter based on the MAD estimate of the noise can be clearly seen in the root
 323 sum of squares (RSS) of the estimates of the two methods (Figure S6). These differences are also
 324 observable in the ATS calculated from estimates obtained with the MAD selection as shown in

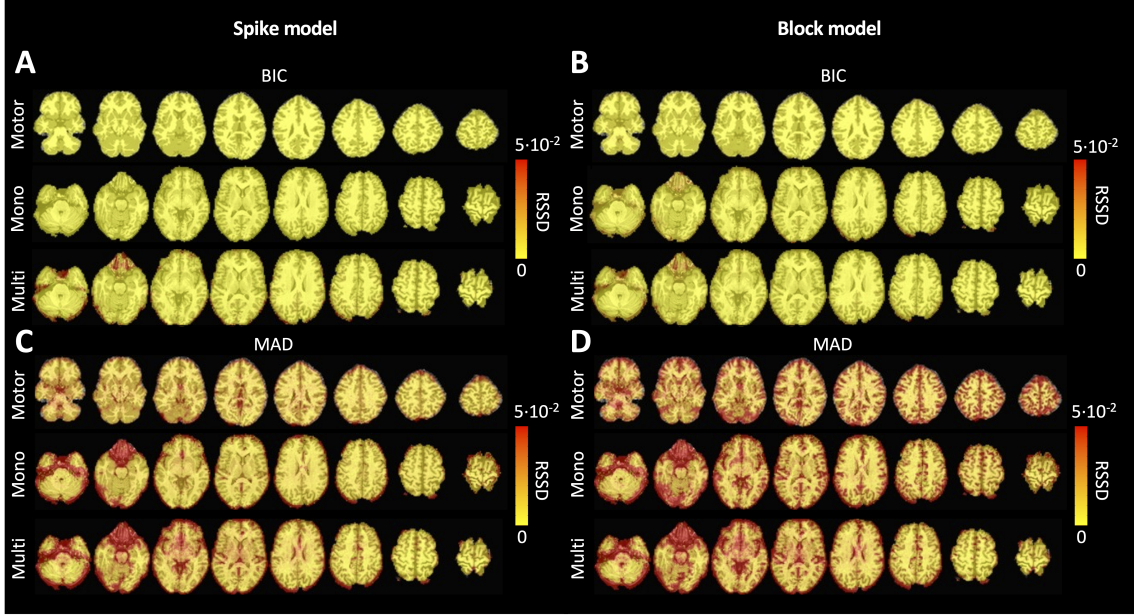


Figure 4: Square root of the sum of squared differences (RSSD) between the estimates obtained with PFM and TA for (A) spike model (activity-inducing signal) and BIC selection of λ , (B) block model (innovation signal) and BIC selection, (C) spike model (activity-inducing signal) and MAD selection, (D) block model (innovation signal) and MAD selection. RSSD maps are shown for the three experimental fMRI datasets: the motor task (Motor), the monoband resting-state (Mono), and the multiband resting-state (Multi) datasets.

325 Figure S9. However, the identical regularization paths shown in Figure S7 demonstrate that both
 326 methods perform equivalently on experimental data (see estimates of innovation signal obtained
 327 with an identical selection of λ in Figure S8). Hence, the higher RSSD values originate from the
 328 different methods to find the optimal regularization parameter based on the MAD estimate of the
 329 noise that yield different solutions as shown by the dashed vertical lines in Figure S7.

330 Figure 5 depicts the results of the analysis of the Motor dataset with the PFM and TA algorithms
 331 using the BIC selection of λ (see Figure S9 for results with MAD selection), as well as a conventional
 332 GLM approach. The Activation Time Series (top left), calculated as the sum of squares of all voxel
 333 amplitudes (positive vs. negative) for a given moment in time, obtained with PFM and TA show
 334 nearly identical patterns. These ATS help to summarize the four dimensional information available
 335 in the results across the spatial domain and identify instances of significant BOLD activity. The
 336 second to sixth rows show the voxel timeseries and the corresponding activity-related, activity-
 337 inducing and innovation signals obtained with PFM using the BIC criterion of representative voxels
 338 in the regions activated in each of the motor tasks. The TA-estimated time-series are not shown
 339 because they were virtually identical. The maps shown on the right correspond to statistical
 340 parametric maps obtained with the GLM for each motor condition ($p < 0.001$) as well as the maps
 341 of the PFM and TA estimates at the onsets of individual motor events (indicated with arrows in
 342 the timecourses). The estimated activity-related, activity-inducing and innovation signals clearly
 343 reveal the activity patterns of each condition in the task, as they exhibit a BOLD response locked to

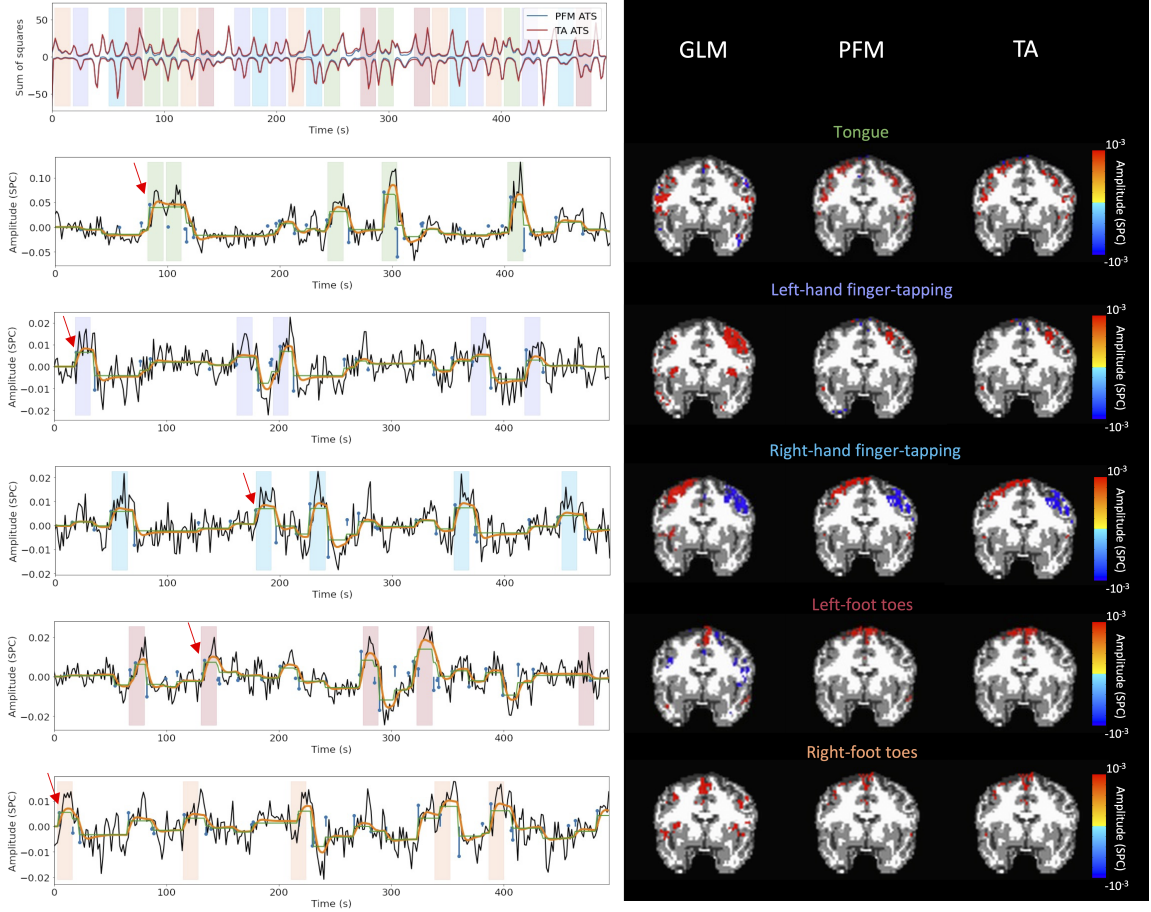


Figure 5: Activity maps of the motor task using a selection of λ based on the BIC estimate. Row 1: Activation time-series (ATS) of the innovation signals estimated by PFM (in blue) or TA (in red) calculated as the sum of squares of all voxels at every timepoint. Positive-valued and negative-valued contributions were separated into two distinct time-courses. Color-bands indicate the onset and duration of each condition in the task (green: tongue motion, purple: left-hand finger-tapping, blue: right-hand finger-tapping, red: left-foot toes motion, orange: right-foot toes motion). Rows 2-6: time-series of a representative voxel for each task with the PFM-estimated innovation (blue), PFM-estimated activity-inducing (green), and activity-related (i.e., fitted, orange) signals, with their corresponding GLM, PFM, and TA maps on the right (representative voxels indicated with green arrows). Amplitudes are given in signal percentage change (SPC). The maps shown on the right are sampled at the time-points labeled with the red arrows and display the innovation signals at these moments across the whole brain.

the onset and duration of the conditions. Overall, activity maps of the innovation signal obtained with PFM and TA highly resemble those obtained with a GLM for individual events, with small differences arising from the distinct specificity of the GLM and deconvolution analyses. Notice that the differences observed with the different approaches to select λ based on the MAD estimate shown in Figure 4 are reflected on the ATS shown in Figure S9 as well.

As an illustration of the insights that deconvolution methods can provide in the analysis of

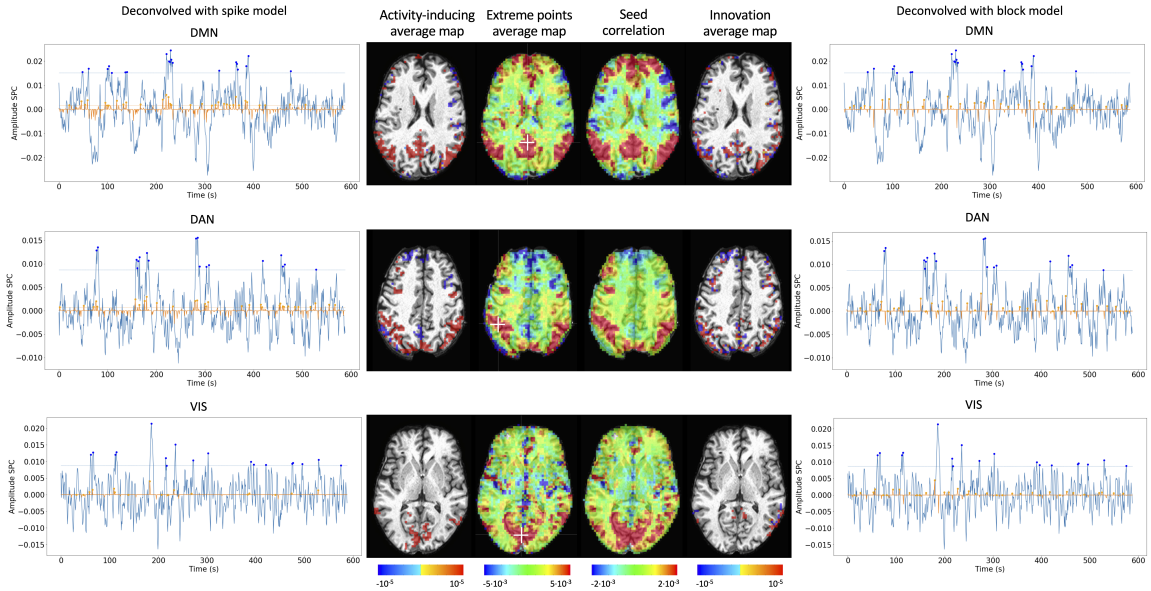


Figure 6: Average activity-inducing (left) and innovation (right) maps obtained from PFM-estimated activity-inducing and innovation signals, respectively, using a BIC-based selection of λ . Time-points selected with a 95th percentile threshold (horizontal lines) are shown over the average time-series (blue) in the seed region (white cross) and the deconvolved signals, i.e., activity inducing (left) and innovation (right) signals (orange). Average maps of extreme points and seed correlation maps are illustrated in the center.

resting-state data, Figure 6 depicts the average activity-inducing and innovation maps of common resting-state networks obtained from thresholding and averaging the activity-inducing and innovation signals, respectively, estimated from the resting-state multiband data using PFM with a selection of λ based on the BIC. The average activity-inducing maps obtained via deconvolution show spatial patterns of the default mode network (DMN), dorsal attention network (DAN), and visual network (VIS) that highly resemble the maps obtained with conventional seed correlation analysis using Pearson's correlation, and the average maps of extreme points of the signal (i.e., with no deconvolution). With deconvolution, the average activity-inducing maps seem to depict more accurate spatial delineation (i.e., less smoothness) than those obtained from the original data, while maintaining the structure of the networks. The BIC-informed selection of λ yields spatial patterns of average activity-inducing and innovation maps that are more sparse than those obtained with a selection of λ based on the MAD estimate (see Figure S10). Furthermore, the spatial patterns of the average innovation maps based on the innovation signals using the block model yield complementary information to those obtained with the activity-inducing signal since iCAPs allow to reveal regions with synchronous innovations, i.e., with the same upregulating and downregulating events. For instance, it is interesting to observe that the structure of the visual network nearly disappears in its corresponding average innovation maps, suggesting the existence of different temporal neuronal patterns across voxels in the primary and secondary visual cortices.

368 **5. Discussion**

369 Hemodynamic deconvolution can be formulated using a synthesis- and analysis-based approach
370 as proposed by PFM and TA, respectively. This work demonstrates that the theoretical equivalence
371 of **both approaches** is confirmed in practice given virtually identical results when the same HRF
372 model and equivalent regularization parameters are employed. Hence, we argue that previously ob-
373 served differences in performance can be explained by specific settings, such as the HRF model and
374 selection of the regularization parameter ([as shown in Figures 4,S6 and S7](#)), convergence thresh-
375 olds, as well as the addition of a spatial regularization term in the spatiotemporal TA formulation
376 ([Karahanoğlu et al., 2013](#)). [For instance, the use of PFM with the spike model in \(Tan et al., 2017\)](#)
377 was seen not to be ideal due to the prolonged trials in the paradigm, which better fit the block
378 model as described here ([7](#)). Similarly, all the works using the iCAPs approach, and thus the TA
379 implementation for deconvolution ([Kinany et al., 2020; Zöller et al., 2019; Pirondini et al., 2022](#)),
380 could alternatively use the PFM approach with the block model adding a spatial regularization
381 term, which would [yield identical results providing the same criterion is used to select the regular-](#)
382 [ization parameters](#). However, given the equivalence of the temporal deconvolution, incorporating
383 extra spatial or temporal regularization terms in the optimization problem should not modify this
384 equivalence providing convex operators are employed. For a convex optimization problem, with
385 a unique global solution, iterative shrinkage thresholding procedures alternating between the dif-
386 ferent regularization terms guarantee convergence; e.g., the generalized forward-backward splitting
387 ([Raguet et al., 2013](#)) algorithm originally employed for TA. Our findings are also in line with the
388 equivalence of analysis and synthesis methods in under-determined cases ($N \leq V$) demonstrated in
389 ([Elad et al., 2007](#)) and ([Ortelli and van de Geer, 2019](#)). [Using a lower regularization parameter \(i.e.,](#)
390 [penalty on the amplitude of the estimates\) makes the estimates more similar to the least-squares](#)
391 [solution, which results in higher sensitivity in detecting events. Conversely, employing a higher](#)
392 [λ leads to higher specificity at the cost of a decrease in sensitivity.](#) Still, we have shown that a
393 slight difference in the selection of the regularization parameter can lead to small differences in the
394 estimated signals when employing the block model with the MAD selection of λ . However, since
395 their regularization paths are equivalent, the algorithms can easily be forced to converge to the
396 same selection of λ , thus resulting in identical estimated signals.

397 Nevertheless, the different formulations of analysis and synthesis deconvolution models bring
398 along different kinds of flexibility. One notable advantage of PFM is that it can readily incorporate
399 any HRF as part of the synthesis operator ([Elad et al., 2007](#)), only requiring the sampled HRF at the
400 desired temporal resolution, which is typically equal to the TR of the acquisition. Conversely, TA
401 relies upon the specification of the discrete differential operator that inverts the HRF, which needs
402 to be derived either by the inverse solution of the sampled HRF impulse response, or by discretizing
403 a continuous-domain differential operator motivated by a biophysical model. The more versatile
404 structure of PFM allows for instance an elegant extension of the algorithm to multi-echo fMRI
405 data ([Caballero-Gaudes et al., 2019](#)) where multiple measurements relate to a common underlying
406 signal. Therefore, the one-to-many synthesis scenario (i.e., from activity-inducing to several activity-
407 related signals) is more cumbersome to express using TA; i.e., a set of differential operators should
408 be defined and the differences between their outputs constrained. Conversely, the one-to-many
409 analysis scenario (i.e., from the measurements to several regularizing signals) is more convenient
410 to be expressed by TA; e.g., combining spike and block regularizers. While the specification of the
411 differential operator in TA only indirectly controls the HRF, the use of the derivative operator to
412 enforce the block model, instead of the integrator in PFM, impacts positively the stability and rate
413 of the convergence of the optimization algorithms. Moreover, analysis formulations can be more

414 suitable for online applications that are still to be explored in fMRI data, but are employed for
415 calcium imaging deconvolution (Friedrich et al., 2017; Jewell et al., 2019), and which have been
416 applied for offline calcium deconvolution (Farouj et al., 2020).

417 Deconvolution techniques can be used before more downstream analysis of brain activity in terms
418 of functional network organization as they estimate interactions between voxels or brain regions that
419 occur at the activity-inducing level, and are thus less affected by the slowness of the hemodynamic
420 response compared to when the BOLD signals are analyzed directly. In addition, deconvolution
421 approaches hold a close parallelism to recent methodologies aiming to understand the dynamics of
422 neuronal activations and interactions at short temporal resolution and that focus on extreme events
423 of the fMRI signal (Lindquist et al., 2007). As an illustration, Figure 6 shows that the innovation-
424 or activity-inducing CAPs computed from deconvolved events in a single resting-state fMRI dataset
425 closely resemble the conventional CAPs computed directly from extreme events of the fMRI signal
426 (Liu and Duyn, 2013; Liu et al., 2013, 2018; Cifre et al., 2020a,b; Zhang et al., 2020; Tagliazucchi
427 et al., 2011, 2012, 2016; Rolls et al., 2021). Similarly, we hypothesize that these extreme events
428 will also show a close resemblance to intrinsic ignition events (Deco and Kringelbach, 2017; Deco
429 et al., 2017). As shown in the maps, deconvolution approaches can offer a more straightforward
430 interpretability of the activation events and resulting functional connectivity patterns. Here, CAPs
431 were computed as the average of spatial maps corresponding to the events of a single dataset.
432 Beyond simple averaging, clustering algorithms (e.g., K-means and consensus clustering) can be
433 employed to discern multiple CAPs or iCAPs at the whole-brain level for a large number of subjects.
434 Previous findings based on iCAPs have for instance revealed organizational principles of brain
435 function during rest (Karahanoglu and Ville, 2015) and sleep (Tarun et al., 2021) in healthy controls,
436 next to alterations in 22q11ds (Zoeller et al., 2019) and multiple sclerosis (Bommarito et al., in
437 press). Next to CAPs-inspired approaches, dynamic functional connectivity has recently been
438 investigated with the use of co-fluctuations and edge-centric techniques (Faskowitz et al., 2020;
439 Esfahlani et al., 2020; Jo et al., 2021; Sporns et al., 2021; van Oort et al., 2018). The activation
440 time series shown in Figure 5 aim to provide equivalent information to the root of sum of squares
441 timecourses used in edge-centric approaches, where timecourses with peaks delineate instances
442 of significant brain activity. Future work could address which type of information is redundant
443 or distinct across these frameworks. In summary, these examples illustrate that deconvolution
444 techniques can be employed prior to other computational approaches and could serve as an effective
445 way of denoising the fMRI data. We foresee an increase in the number of studies that take advantage
446 of the potential benefits of using deconvolution methods prior to functional connectivity analyses.

447 In sum, hemodynamic deconvolution approaches using sparsity-driven regularization are valuable
448 tools to complete the fMRI processing pipeline. Although the two approaches examined in
449 detail here provide alternative representations of the BOLD signals in terms of innovation and
450 activity-inducing signals, their current implementations have certain limitations, calling for further
451 developments or more elaborate models, where some of them have been initially addressed in the
452 literature. One relevant focus is to account for the variability in HRF that can be observed in
453 different regions of the brain. First, variability in the temporal characteristics of the HRF can arise
454 from differences in stimulus intensity and patterns, as well as with short inter-event intervals like in
455 fast cognitive processes or experimental designs (Yeşilyurt et al., 2008; Chen et al., 2021; Sadaghiani
456 et al., 2009; Polimeni and Lewis, 2021). Similarly, the HRF shape at rest might differ from the
457 canonical HRF commonly used for task-based fMRI data analysis. A wide variety of HRF patterns
458 could be elicited across the whole brain and possible detected with sufficiently large signal-to-noise
459 ratio, e.g., (Gonzalez-Castillo et al., 2012) showed two gamma-shaped responses at the onset and

460 the end of the evoked trial, respectively. This unique HRF shape would be deconvolved as two
461 separate events with the conventional deconvolution techniques. The impact of HRF variability
462 could be reduced using structured regularization terms along with multiple basis functions (Gaudes
463 et al., 2012) or procedures that estimate the HRF shape in an adaptive fashion in both analysis
464 (Farouj et al., 2019) and synthesis formulations (Cherkaoui et al., 2020a).

465 Another avenue of research consists in leveraging spatial information by adopting multivariate
466 deconvolution approaches that operate at the whole-brain level, instead of working voxelwise and
467 beyond regional regularization terms (e.g. as proposed in Karahanoglu et al. 2013). Operating
468 at the whole-brain level would open the way for methods that consider shared neuronal activity
469 using mixed norm regularization terms (Uruñuela-Tremiño et al., 2019) or can capture long-range
470 neuronal cofluctuations using low rank decompositions (Cherkaoui et al., 2020a). For example,
471 multivariate deconvolution approaches could yield better localized activity patterns while reducing
472 the effect of global fluctuations such as respiratory artifacts, which cannot be modelled at the voxel
473 level (Uruñuela et al., 2021).

474 Similar to solving other inverse problems by means of regularized estimators, the selection of
475 the regularization parameter is critical to correctly estimate the neuronal-related signal. Hence,
476 methods that take advantage of a more robust selection of the regularization parameter could
477 considerably yield more reliable estimates of the neuronal-related signal. For instance, the stability
478 selection (Meinshausen and Bühlmann, 2010; Uruñuela et al., 2020) procedure could be included
479 to the deconvolution problem to ensure that the estimated coefficients are obtained with high
480 probability. Furthermore, an important issue of regularized estimation is that the estimates are
481 biased with respect to the true value. In that sense, the use of non-convex $\ell_{p,q}$ -norm regularization
482 terms (e.g., $p < 1$) can reduce this bias while maintaining the sparsity constraint, at the cost of
483 potentially converging to a local minima of the regularized estimation problem. In practice, these
484 approaches could avoid the optional debiasing step that overcomes the shrinkage of the estimates and
485 obtain a more accurate and less biased fit of the fMRI signal (Gaudes et al., 2013; Caballero-Gaudes
486 et al., 2019). Finally, cutting-edge developments on physics-informed deep learning techniques
487 for inverse problems (Akçakaya et al., 2021; Monga et al., 2021; Ongie et al., 2020; Cherkaoui
488 et al., 2020b) could be transferred for deconvolution by considering the biophysical model of the
489 hemodynamic system and could potentially offer algorithms with reduced computational time and
490 more flexibility.

491 6. Code and data availability

492 The code and materials used in this work can be found in the following GitHub repository:
493 https://github.com/eurunuela/pfm_vs_ta. We encourage the reader to explore the parameters
494 (e.g., SNR, varying HRF options and mismatch between algorithms, TR, number of events, onsets,
495 and durations) in the provided Jupyter notebooks. Likewise, the data used to produce the figures
496 can be found in <https://osf.io/f3ryg/>.

497 7. Acknowledgements

498 We thank Stefano Moia and Vicente Ferrer for data availability, and Younes Farouj for valuable
499 comments on the manuscript. This research was funded by the Spanish Ministry of Economy and
500 Competitiveness (RYC-2017-21845), the Basque Government (BERC 2018-2021, PIB_2019_104,
501 PRE_2020_2_0227), and the Spanish Ministry of Science, Innovation and Universities (PID2019-
502 105520GB-100), and the Swiss National Science Foundation (grant 205321_163376).

503 **8. CRediT**

504 Eneko Uruñuela: Conceptualisation, Methodology, Software, Formal Analysis, Investigation,
505 Data Curation, Writing (OD), Writing (RE), Visualisation, Funding acquisition. Thomas A.W.
506 Bolton: Conceptualisation, Methodology, Writing (RE). Dimitri Van de Ville: Conceptualisation,
507 Methodology, Writing (RE). César Caballero-Gaudes: Conceptualisation, Methodology, Software,
508 Formal Analysis, Investigation, Data Curation, Writing (OD), Writing (RE), Visualisation, Funding
509 acquisition.

510 **References**

- 511 Akçakaya, M., Yaman, B., Chung, H., Ye, J.C., 2021. Unsupervised deep learning methods for
512 biological image reconstruction [arXiv:2105.08040](https://arxiv.org/abs/2105.08040).
- 513 Allan, T.W., Francis, S.T., Caballero-Gaudes, C., Morris, P.G., Liddle, E.B., Liddle, P.F., Brookes,
514 M.J., Gowland, P.A., 2015. Functional connectivity in MRI is driven by spontaneous BOLD
515 events. *PLOS ONE* 10, e0124577. doi:10.1371/journal.pone.0124577.
- 516 Andersson, J.L., Skare, S., Ashburner, J., 2003. How to correct susceptibility distortions in spin-
517 echo echo-planar images: application to diffusion tensor imaging. *NeuroImage* 20, 870–888.
518 doi:10.1016/s1053-8119(03)00336-7.
- 519 Aslan, S., Cemgil, A.T., Akin, A., 2016. Joint state and parameter estimation of the hemodynamic
520 model by particle smoother expectation maximization method. *Journal of Neural Engineering*
521 13, 046010. doi:10.1088/1741-2560/13/4/046010.
- 522 Beck, A., Teboulle, M., 2009. A fast iterative shrinkage-thresholding algorithm for linear inverse
523 problems. *SIAM Journal on Imaging Sciences* 2, 183–202. doi:10.1137/080716542.
- 524 Behzadi, Y., Restom, K., Liau, J., Liu, T.T., 2007. A component based noise correction method
525 (CompCor) for BOLD and perfusion based fMRI. *NeuroImage* 37, 90–101. doi:10.1016/j.
526 neuroimage.2007.04.042.
- 527 Birn, R.M., Diamond, J.B., Smith, M.A., Bandettini, P.A., 2006. Separating respiratory-variation-
528 related fluctuations from neuronal-activity-related fluctuations in fMRI. *NeuroImage* 31, 1536–
529 1548. doi:10.1016/j.neuroimage.2006.02.048.
- 530 Bommarito, G., Tarun, A., Farouj, Y., Preti, M.G., Petracca, M., Droby, A., Mendili, M.M.E.,
531 Inglese, M., Ville, D.V.D., 2020. Altered anterior default mode network dynamics in progressive
532 multiple sclerosis. *medRxiv* doi:10.1101/2020.11.26.20238923.
- 533 Bommarito, G., Tarun, A., Farouj, Y., Preti, M.G., Petracca, M., Droby, A., Mounir El Mendili,
534 M., Inglese, M., Van De Ville, D., in press. Altered anterior default mode network dynamics in
535 progressive multiple sclerosis. *Multiple Sclerosis Journal* doi:10.1177/13524585211018116.
- 536 Boynton, G.M., Engel, S.A., Glover, G.H., Heeger, D.J., 1996. Linear systems analysis of functional
537 magnetic resonance imaging in human v1. *The Journal of Neuroscience* 16, 4207–4221. doi:10.
538 1523/jneurosci.16-13-04207.1996.

- 539 Bruckstein, A.M., Donoho, D.L., Elad, M., 2009. From sparse solutions of systems of equations to
540 sparse modeling of signals and images. *SIAM Review* 51, 34–81. doi:10.1137/060657704.
- 541 Bush, K., Cisler, J., 2013. Decoding neural events from fMRI BOLD signal: A comparison of
542 existing approaches and development of a new algorithm. *Magnetic Resonance Imaging* 31, 976–
543 989. doi:10.1016/j.mri.2013.03.015.
- 544 Bush, K., Zhou, S., Cisler, J., Bian, J., Hazaroglu, O., Gillispie, K., Yoshigoe, K., Kilts, C.,
545 2015. A deconvolution-based approach to identifying large-scale effective connectivity. *Magnetic*
546 *Resonance Imaging* 33, 1290–1298. doi:10.1016/j.mri.2015.07.015.
- 547 Buxton, R.B., Wong, E.C., Frank, L.R., 1998. Dynamics of blood flow and oxygenation changes
548 during brain activation: the balloon model. *Magnetic resonance in medicine* 39, 855–864.
- 549 Caballero-Gaudes, C., Moia, S., Panwar, P., Bandettini, P.A., Gonzalez-Castillo, J., 2019. A
550 deconvolution algorithm for multi-echo functional MRI: Multi-echo sparse paradigm free mapping.
551 *NeuroImage* 202, 116081. doi:10.1016/j.neuroimage.2019.116081.
- 552 Casanova, R., Ryali, S., Serences, J., Yang, L., Kraft, R., Laurienti, P.J., Maldjian, J.A., 2008. The
553 impact of temporal regularization on estimates of the BOLD hemodynamic response function: A
554 comparative analysis. *NeuroImage* 40, 1606–1618. doi:10.1016/j.neuroimage.2008.01.011.
- 555 Chambolle, A., 2004. An algorithm for total variation minimization and applications. *Journal of*
556 *Mathematical imaging and vision* 20, 89–97.
- 557 Chen, J.E., Glover, G.H., Fultz, N.E., Rosen, B.R., Polimeni, J.R., Lewis, L.D., 2021. Investigating
558 mechanisms of fast BOLD responses: The effects of stimulus intensity and of spatial heterogeneity
559 of hemodynamics. *NeuroImage* 245, 118658. doi:10.1016/j.neuroimage.2021.118658.
- 560 Chen, S.S., Donoho, D.L., Saunders, M.A., 2001. Atomic decomposition by basis pursuit. *SIAM*
561 *review* 43, 129–159.
- 562 Cherkaoui, H., Moreau, T., Halimi, A., Ciuciu, P., 2019. Sparsity-based blind deconvolution of
563 neural activation signal in FMRI, in: *ICASSP 2019 - 2019 IEEE International Conference on*
564 *Acoustics, Speech and Signal Processing (ICASSP)*, IEEE. pp. 1323–1327. doi:10.1109/icassp.
565 2019.8683358.
- 566 Cherkaoui, H., Moreau, T., Halimi, A., Leroy, C., Ciuciu, P., 2020a. Multivariate semi-blind
567 deconvolution of fMRI time series. URL: <https://hal.archives-ouvertes.fr/hal-03005584>.
568 working paper or preprint.
- 569 Cherkaoui, H., Sulam, J., Moreau, T., 2020b. Learning to solve TV regularised problems with
570 unrolled algorithms 33, 11513–11524. URL: <https://proceedings.neurips.cc/paper/2020/file/84fec9a8e45846340fdf5c7c9f7ed66c-Paper.pdf>.
- 572 Cifre, I., Flores, M.T.M., Ochab, J.K., Chialvo, D.R., 2020a. Revisiting non-linear functional brain
573 co-activations: directed, dynamic and delayed. *arXiv:2007.15728*.
- 574 Cifre, I., Zarepour, M., Horovitz, S.G., Cannas, S.A., Chialvo, D.R., 2020b. Further results on why
575 a point process is effective for estimating correlation between brain regions. *Papers in Physics*
576 12, 120003. doi:10.4279/PIP.120003.

- 577 Ciuciu, P., Poline, J.B., Marrelec, G., Idier, J., Pallier, C., Benali, H., 2003. Unsupervised robust
578 nonparametric estimation of the hemodynamic response function for any fmri experiment. IEEE
579 transactions on medical imaging 22, 1235–1251. doi:10.1109/TMI.2003.817759.
- 580 Cohen, M.S., 1997. Parametric analysis of fMRI data using linear systems methods. NeuroImage
581 6, 93–103. doi:10.1006/nimg.1997.0278.
- 582 Costantini, I., Deriche, R., Deslauriers-Gauthier, S., 2021. A paradigm free regularization approach
583 to recover brain activation from functional MRI data. bioRxiv doi:10.1101/2021.04.14.438942.
- 584 Cox, R.W., 1996. AFNI: Software for analysis and visualization of functional magnetic resonance
585 neuroimages. Computers and Biomedical Research 29, 162–173. doi:10.1006/cbmr.1996.0014.
- 586 Deco, G., Kringelbach, M.L., 2017. Hierarchy of information processing in the brain: A novel
587 ‘intrinsic ignition’ framework. Neuron 94, 961–968. doi:10.1016/j.neuron.2017.03.028.
- 588 Deco, G., Tagliazucchi, E., Laufs, H., Sanjuán, A., Kringelbach, M.L., 2017. Novel intrinsic ignition
589 method measuring local-global integration characterizes wakefulness and deep sleep. eNeuro 4.
590 doi:10.1523/ENEURO.0106-17.2017.
- 591 Di, X., Biswal, B.B., 2013. Modulatory interactions of resting-state brain functional connectivity.
592 PLoS ONE 8, e71163. doi:10.1371/journal.pone.0071163.
- 593 Di, X., Biswal, B.B., 2015. Characterizations of resting-state modulatory interactions in the human
594 brain. Journal of Neurophysiology 114, 2785–2796. doi:10.1152/jn.00893.2014.
- 595 Di, X., Biswal, B.B., 2018. Toward task connectomics: Examining whole-brain task modulated
596 connectivity in different task domains. Cerebral Cortex 29, 1572–1583. doi:10.1093/cercor/
597 bhy055.
- 598 Efron, B., Hastie, T., Johnstone, I., Tibshirani, R., 2004. Least angle regression. The Annals of
599 Statistics 32, 407–499. doi:10.1214/009053604000000067.
- 600 Elad, M., Milanfar, P., Rubinstein, R., 2007. Analysis versus synthesis in signal priors. Inverse
601 Problems 23, 947–968. doi:10.1088/0266-5611/23/3/007.
- 602 Esfahlani, F.Z., Jo, Y., Faskowitz, J., Byrge, L., Kennedy, D.P., Sporns, O., Betzel, R.F., 2020.
603 High-amplitude cofluctuations in cortical activity drive functional connectivity. Proceedings of
604 the National Academy of Sciences 117, 28393–28401. doi:10.1073/pnas.2005531117.
- 605 Farouj, Y., Karahanoglu, F.I., Ville, D.V.D., 2019. Bold signal deconvolution under uncertain
606 hEmodynamics: A semi-blind approach, in: 2019 IEEE 16th International Symposium on
607 Biomedical Imaging (ISBI 2019), IEEE. IEEE. pp. 1792–1796. doi:10.1109/isbi.2019.8759248.
- 608 Farouj, Y., Karahanoglu, F.I., Ville, D.V.D., 2020. Deconvolution of sustained neural activity from
609 large-scale calcium imaging data 39, 1094–1103. doi:10.1109/tmi.2019.2942765.
- 610 Faskowitz, J., Esfahlani, F.Z., Jo, Y., Sporns, O., Betzel, R.F., 2020. Edge-centric functional
611 network representations of human cerebral cortex reveal overlapping system-level architecture.
612 Nature neuroscience 23, 1644–1654. doi:10.1038/s41593-020-00719-y.

- 613 Feinberg, D.A., Moeller, S., Smith, S.M., Auerbach, E., Ramanna, S., Glasser, M.F., Miller, K.L.,
614 Ugurbil, K., Yacoub, E., 2010. Multiplexed echo planar imaging for sub-second whole brain
615 fMRI and fast diffusion imaging. PLoS ONE 5, e15710. doi:10.1371/journal.pone.0015710.
- 616 Freitas, L.G., Bolton, T.A., Krikler, B.E., Jochaut, D., Giraud, A.L., Hüppi, P.S., Ville, D.V.D.,
617 2020. Time-resolved effective connectivity in task fMRI: Psychophysiological interactions of co-
618 activation patterns. NeuroImage 212, 116635. doi:10.1016/j.neuroimage.2020.116635.
- 619 Friedrich, J., Zhou, P., Paninski, L., 2017. Fast online deconvolution of calcium imaging data.
620 PLOS Computational Biology 13, e1005423. doi:10.1371/journal.pcbi.1005423.
- 621 Friston, K., Fletcher, P., Josephs, O., Holmes, A., Rugg, M., Turner, R., 1998. Event-related fMRI:
622 Characterizing differential responses. NeuroImage 7, 30–40. doi:10.1006/nimg.1997.0306.
- 623 Friston, K., Trujillo-Barreto, N., Daunizeau, J., 2008. DEM: A variational treatment of dynamic
624 systems. NeuroImage 41, 849–885. doi:10.1016/j.neuroimage.2008.02.054.
- 625 Friston, K.J., Jezzard, P., Turner, R., 1994. Analysis of functional MRI time-series. Human Brain
626 Mapping 1, 153–171. doi:10.1002/hbm.460010207.
- 627 Friston, K.J., Mechelli, A., Turner, R., Price, C.J., 2000. Nonlinear responses in fmri: the balloon
628 model, volterra kernels, and other hemodynamics. NeuroImage 12, 466–477.
- 629 Gaudes, C.C., Karahanoglu, F.I., Lazeyras, F., Ville, D.V.D., 2012. Structured sparse deconvolution
630 for paradigm free mapping of functional MRI data, in: 2012 9th IEEE International Symposium
631 on Biomedical Imaging (ISBI), IEEE. IEEE. pp. 322–325. doi:10.1109/isbi.2012.6235549.
- 632 Gaudes, C.C., Petridou, N., Dryden, I.L., Bai, L., Francis, S.T., Gowland, P.A., 2010. Detection
633 and characterization of single-trial fMRI bold responses: Paradigm free mapping. Human Brain
634 Mapping 32, 1400–1418. doi:10.1002/hbm.21116.
- 635 Gaudes, C.C., Petridou, N., Francis, S.T., Dryden, I.L., Gowland, P.A., 2013. Paradigm free
636 mapping with sparse regression automatically detects single-trial functional magnetic resonance
637 imaging blood oxygenation level dependent responses. Human Brain Mapping , n/a–n/adoi:10.
638 1002/hbm.21452.
- 639 Gaudes, C.C., Van De Ville, D., Petridou, N., Lazeyras, F., Gowland, P., 2011. Paradigm-free
640 mapping with morphological component analysis: Getting most out of fmri data, in: Wavelets
641 and Sparsity XIV, International Society for Optics and Photonics. p. 81381K.
- 642 Gerchen, M.F., Bernal-Casas, D., Kirsch, P., 2014. Analyzing task-dependent brain network changes
643 by whole-brain psychophysiological interactions: A comparison to conventional analysis. Human
644 Brain Mapping 35, 5071–5082. doi:10.1002/hbm.22532.
- 645 Gitelman, D.R., Penny, W.D., Ashburner, J., Friston, K.J., 2003. Modeling regional and psy-
646 chophysiological interactions in fMRI: the importance of hemodynamic deconvolution. NeuroImage
647 19, 200–207. doi:10.1016/s1053-8119(03)00058-2.
- 648 Glasser, M.F., Smith, S.M., Marcus, D.S., Andersson, J.L.R., Auerbach, E.J., Behrens, T.E.J.,
649 Coalson, T.S., Harms, M.P., Jenkinson, M., Moeller, S., Robinson, E.C., Sotiroopoulos, S.N., Xu,
650 J., Yacoub, E., Ugurbil, K., Essen, D.C.V., 2016. The human connectome project's neuroimaging
651 approach. Nature Neuroscience 19, 1175–1187. doi:10.1038/nn.4361.

- 652 Glover, G.H., 1999. Deconvolution of impulse response in event-related BOLD fMRI1. NeuroImage
653 9, 416–429. doi:10.1006/nimg.1998.0419.
- 654 Gonzalez-Castillo, J., Caballero-Gaudes, C., Topolski, N., Handwerker, D.A., Pereira, F., Ban-
655 dettini, P.A., 2019. Imaging the spontaneous flow of thought: Distinct periods of cogni-
656 tion contribute to dynamic functional connectivity during rest. NeuroImage 202, 116129.
657 doi:10.1016/j.neuroimage.2019.116129.
- 658 Gonzalez-Castillo, J., Saad, Z.S., Handwerker, D.A., Inati, S.J., Brenowitz, N., Bandettini, P.A.,
659 2012. Whole-brain, time-locked activation with simple tasks revealed using massive averaging
660 and model-free analysis. Proceedings of the National Academy of Sciences of the United States
661 of America 109, 5487–5492. doi:10.1073/pnas.1121049109.
- 662 Goutte, C., Nielsen, F.A., Hansen, L.K., 2000. Modeling the haemodynamic response in fmri using
663 smooth fir filters. IEEE transactions on medical imaging 19, 1188–1201. doi:10.1109/42.897811.
- 664 Havlicek, M., Friston, K.J., Jan, J., Brazdil, M., Calhoun, V.D., 2011. Dynamic modeling of
665 neuronal responses in fMRI using cubature kalman filtering. NeuroImage 56, 2109–2128. doi:10.
666 1016/j.neuroimage.2011.03.005.
- 667 Henson, R., Friston, K., 2007. Chapter 14 - convolution models for fmri, in: Friston, K., Ash-
668 burner, J., Kiebel, S., Nichols, T., Penny, W. (Eds.), Statistical Parametric Mapping. Academic
669 Press, London, pp. 178–192. URL: <https://www.sciencedirect.com/science/article/pii/B9780123725608500140>, doi:<https://doi.org/10.1016/B978-012372560-8/50014-0>.
- 671 Hernandez-Garcia, L., Ulfarsson, M.O., 2011. Neuronal event detection in fMRI time series using
672 iterative deconvolution techniques. Magnetic Resonance Imaging 29, 353–364. doi:10.1016/j.j.
673 mri.2010.10.012.
- 674 Hütel, M., Antonelli, M., Melbourne, A., Ourselin, S., 2021. Hemodynamic matrix factorization for
675 functional magnetic resonance imaging. NeuroImage 231, 117814. doi:10.1016/j.neuroimage.
676 2021.117814.
- 677 Hütel, M., Melbourne, A., Ourselin, S., 2018. Neural activation estimation in brain networks
678 during task and rest using BOLD-fMRI, in: Medical Image Computing and Computer Assisted
679 Intervention – MICCAI 2018, Springer. Springer International Publishing. pp. 215–222. doi:10.
680 1007/978-3-030-00931-1_25.
- 681 Jenkinson, M., Beckmann, C.F., Behrens, T.E., Woolrich, M.W., Smith, S.M., 2012. FSL. Neu-
682 roImage 62, 782–790. doi:10.1016/j.neuroimage.2011.09.015.
- 683 Jenkinson, M., Smith, S., 2001. A global optimisation method for robust affine registration of brain
684 images. Medical Image Analysis 5, 143–156. doi:10.1016/s1361-8415(01)00036-6.
- 685 Jewell, S.W., Hocking, T.D., Fearnhead, P., Witten, D.M., 2019. Fast nonconvex deconvolution of
686 calcium imaging data. Biostatistics 21, 709–726. doi:10.1093/biostatistics/kxy083.
- 687 Jo, Y., Faskowitz, J., Esfahlani, F.Z., Sporns, O., Betzel, R.F., 2021. Subject identification us-
688 ing edge-centric functional connectivity. NeuroImage 238, 118204. doi:10.1016/j.neuroimage.
689 2021.118204.

- 690 Karahanoglu, F.I., Bayram, İ., Ville, D.V.D., 2011. A signal processing approach to generalized
691 1-d total variation. *IEEE Transactions on Signal Processing* 59, 5265–5274. doi:10.1109/tsp.
692 2011.2164399.
- 693 Karahanoglu, F.I., Caballero-Gaudes, C., Lazeyras, F., Ville, D.V.D., 2013. Total activation: fMRI
694 deconvolution through spatio-temporal regularization. *NeuroImage* 73, 121–134. doi:10.1016/
695 j.neuroimage.2013.01.067.
- 696 Karahanoglu, F.I., Grouiller, F., Gaudes, C.C., Seeck, M., Vulliemoz, S., Ville, D.V.D., 2013.
697 Spatial mapping of interictal epileptic discharges in fMRI with total activation, in: 2013 IEEE
698 10th International Symposium on Biomedical Imaging, Ieee. IEEE. pp. 1500–1503. doi:10.1109/
699 isbi.2013.6556819.
- 700 Karahanoglu, F.I., Ville, D.V.D., 2015. Transient brain activity disentangles fMRI resting-state
701 dynamics in terms of spatially and temporally overlapping networks. *Nature Communications* 6,
702 7751. doi:10.1038/ncomms8751.
- 703 Karahanoglu, F.I., Ville, D.V.D., 2017. Dynamics of large-scale fMRI networks: Deconstruct brain
704 activity to build better models of brain function. *Current Opinion in Biomedical Engineering* 3,
705 28–36. doi:10.1016/j.cobme.2017.09.008.
- 706 Keilholz, S., Caballero-Gaudes, C., Bandettini, P., Deco, G., Calhoun, V., 2017. Time-resolved
707 resting-state functional magnetic resonance imaging analysis: Current status, challenges, and
708 new directions. *Brain Connectivity* 7, 465–481. doi:10.1089/brain.2017.0543.
- 709 Khalidov, I., Fadili, J., Lazeyras, F., Ville, D.V.D., Unser, M., 2011. Activelets: Wavelets for
710 sparse representation of hemodynamic responses. *Signal Processing* 91, 2810–2821. doi:10.1016/
711 j.sigpro.2011.03.008.
- 712 Kinany, N., Pirondini, E., Micera, S., Ville, D.V.D., 2020. Dynamic functional connectivity of
713 resting-state spinal cord fMRI reveals fine-grained intrinsic architecture. *Neuron* 108, 424–435.e4.
714 doi:10.1016/j.neuron.2020.07.024.
- 715 Lindquist, M.A., Waugh, C., Wager, T.D., 2007. Modeling state-related fMRI activity using change-
716 point theory. *NeuroImage* 35, 1125–1141. doi:10.1016/j.neuroimage.2007.01.004.
- 717 Liu, X., Chang, C., Duyn, J.H., 2013. Decomposition of spontaneous brain activity into distinct
718 fMRI co-activation patterns. *Frontiers in Systems Neuroscience* 7, 101. doi:10.3389/fnsys.
719 2013.00101.
- 720 Liu, X., Duyn, J.H., 2013. Time-varying functional network information extracted from brief
721 instances of spontaneous brain activity. *Proceedings of the National Academy of Sciences* 110,
722 4392–4397. doi:10.1073/pnas.1216856110.
- 723 Liu, X., Zhang, N., Chang, C., Duyn, J.H., 2018. Co-activation patterns in resting-state fMRI
724 signals. *NeuroImage* 180, 485–494. doi:10.1016/j.neuroimage.2018.01.041.
- 725 Lopes, R., Lina, J., Fahoum, F., Gotman, J., 2012. Detection of epileptic activity in fMRI without
726 recording the EEG. *NeuroImage* 60, 1867–1879. doi:10.1016/j.neuroimage.2011.12.083.

- 727 Loula, J., Varoquaux, G., Thirion, B., 2018. Decoding fMRI activity in the time domain improves
728 classification performance. *NeuroImage* 180, 203–210. doi:10.1016/j.neuroimage.2017.08.018.
- 729 Lurie, D.J., Kessler, D., Bassett, D.S., Betzel, R.F., Breakspear, M., Kheilholz, S., Kucyi, A.,
730 Liégeois, R., Lindquist, M.A., McIntosh, A.R., Poldrack, R.A., Shine, J.M., Thompson, W.H.,
731 Bielczyk, N.Z., Douw, L., Kraft, D., Miller, R.L., Muthuraman, M., Pasquini, L., Razi, A.,
732 Vidaurre, D., Xie, H., Calhoun, V.D., 2020. Questions and controversies in the study of time-
733 varying functional connectivity in resting fMRI. *Network Neuroscience* 4, 30–69. doi:10.1162/
734 netn_a_00116.
- 735 Madi, M.K., Karameh, F.N., 2017. Hybrid cubature kalman filtering for identifying nonlinear
736 models from sampled recording: Estimation of neuronal dynamics. *PLOS ONE* 12, e0181513.
737 doi:10.1371/journal.pone.0181513.
- 738 Marrelec, G., Benali, H., Ciuci, P., Poline, J.B., 2002. Bayesian estimation of the hemo-
739 dynamic response function in functional mri. *AIP Conference Proceedings* 617, 229–247.
740 URL: <https://aip.scitation.org/doi/abs/10.1063/1.1477050>, doi:10.1063/1.1477050,
741 arXiv:<https://aip.scitation.org/doi/pdf/10.1063/1.1477050>.
- 742 Meinshausen, N., Bühlmann, P., 2010. Stability selection. *Journal of the Royal Statistical Society:*
743 *Series B (Statistical Methodology)* 72, 417–473. doi:10.1111/j.1467-9868.2010.00740.x.
- 744 Moeller, S., Yacoub, E., Olman, C.A., Auerbach, E., Strupp, J., Harel, N., Uğurbil, K., 2010.
745 Multiband multislice GE-EPI at 7 tesla, with 16-fold acceleration using partial parallel imaging
746 with application to high spatial and temporal whole-brain fMRI. *Magnetic Resonance in Medicine*
747 63, 1144–1153. doi:10.1002/mrm.22361.
- 748 Monga, V., Li, Y., Eldar, Y.C., 2021. Algorithm unrolling: Interpretable, efficient deep learning
749 for signal and image processing. *IEEE Signal Processing Magazine* 38, 18–44. doi:10.1109/MSP.
750 2020.3016905.
- 751 Ongie, G., Jalal, A., Metzler, C.A., Baraniuk, R.G., Dimakis, A.G., Willett, R., 2020. Deep learning
752 techniques for inverse problems in imaging. *IEEE Journal on Selected Areas in Information
753 Theory* 1, 39–56. doi:10.1109/JSAIT.2020.2991563.
- 754 van Oort, E.S.B., Mennes, M., Navarro Schröder, T., Kumar, V.J., Zaragoza Jimenez, N.I., Grodd,
755 W., Doeller, C.F., Beckmann, C.F., 2018. Functional parcellation using time courses of instant-
756 taneous connectivity. *NeuroImage* 170, 31–40. doi:10.1016/j.neuroimage.2017.07.027.
- 757 Ortelli, F., van de Geer, S., 2019. Synthesis and analysis in total variation regularization.
758 arXiv:1901.06418.
- 759 Patriat, R., Molloy, E.K., Birn, R.M., 2015. Using edge voxel information to improve motion
760 regression for rs-fMRI connectivity studies. *Brain Connectivity* 5, 582–595. doi:10.1089/brain.
761 2014.0321.
- 762 Penny, W., Ghahramani, Z., Friston, K., 2005. Bilinear dynamical systems. *Philosophical Trans-
763 actions of the Royal Society B: Biological Sciences* 360, 983–993. doi:10.1098/rstb.2005.1642.

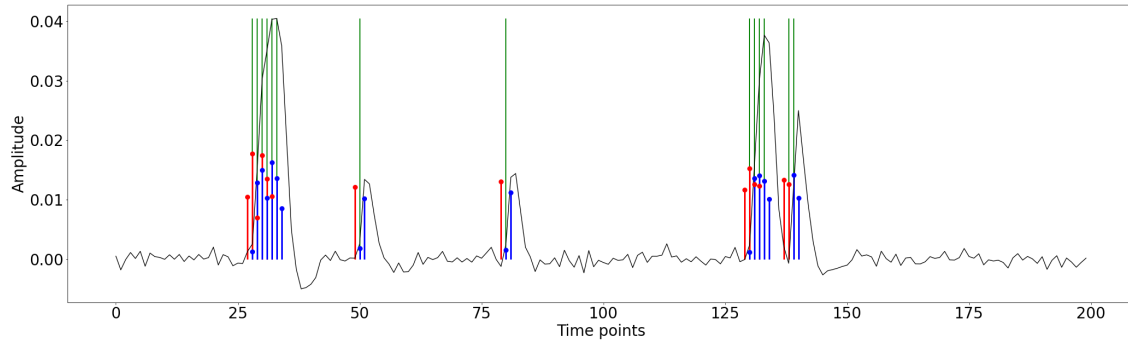
- 764 Petridou, N., Gaudes, C.C., Dryden, I.L., Francis, S.T., Gowland, P.A., 2012. Periods of rest in
765 fMRI contain individual spontaneous events which are related to slowly fluctuating spontaneous
766 activity. *Human Brain Mapping* 34, 1319–1329. doi:10.1002/hbm.21513.
- 767 Pidnebesna, A., Fajnerová, I., Horáček, J., Hlinka, J., 2019. Estimating sparse neuronal signal from
768 hemodynamic response: the mixture components inference approach. *bioRxiv* doi:10.1101/2019.
769 12.19.876508.
- 770 Pirondini, E., Kinany, N., Sueur, C.L., Griffis, J.C., Shulman, G.L., Corbetta, M., Ville, D.V.D.,
771 2022. Post-stroke reorganization of transient brain activity characterizes deficits and recovery of
772 cognitive functions. *NeuroImage* 255, 119201. doi:10.1016/j.neuroimage.2022.119201.
- 773 Polimeni, J.R., Lewis, L.D., 2021. Imaging faster neural dynamics with fast fmri: A need for
774 updated models of the hemodynamic response. *Progress in neurobiology* 207, 102174. doi:10.
775 1016/j.pneurobio.2021.102174.
- 776 Posse, S., Wiese, S., Gembbris, D., Mathiak, K., Kessler, C., Grosse-Ruyken, M.L., Elghahwagi,
777 B., Richards, T., Dager, S.R., Kiselev, V.G., 1999. Enhancement of BOLD-contrast sensitivity
778 by single-shot multi-echo functional MR imaging. *Magnetic Resonance in Medicine* 42, 87–97.
779 doi:10.1002/(sici)1522-2594(199907)42:1<87::aid-mrm13>3.0.co;2-o.
- 780 Preti, M.G., Bolton, T.A., Ville, D.V.D., 2017. The dynamic functional connectome: State-of-the-
781 art and perspectives. *NeuroImage* 160, 41–54. doi:10.1016/j.neuroimage.2016.12.061.
- 782 Raguet, H., Fadili, J., Peyré, G., 2013. A generalized forward-backward splitting. *SIAM Journal*
783 on Imaging Sciences 6, 1199–1226. doi:10.1137/120872802.
- 784 Riera, J.J., Watanabe, J., Kazuki, I., Naoki, M., Aubert, E., Ozaki, T., Kawashima, R., 2004. A
785 state-space model of the hemodynamic approach: nonlinear filtering of BOLD signals. *NeuroIm-*
786 *age* 21, 547–567. doi:10.1016/j.neuroimage.2003.09.052.
- 787 Rolls, E.T., Cheng, W., Feng, J., 2021. Brain dynamics: Synchronous peaks, functional connectivity,
788 and its temporal variability. *Human brain mapping* 42, 2790–2801. doi:10.1002/hbm.25404.
- 789 Ruiz-Euler, H.C., Marques, J.R.F., Kappen, H.J., 2018. Nonlinear deconvolution by sampling
790 biophysically plausible hemodynamic models. *arXiv:1803.08797*.
- 791 Sadaghiani, S., Uğurbil, K., Uludağ, K., 2009. Neural activity-induced modulation of bold poststim-
792 ulus undershoot independent of the positive signal. *Magnetic resonance imaging* 27, 1030–1038.
793 doi:10.1016/j.mri.2009.04.003.
- 794 Schwarz, G., 1978. Estimating the dimension of a model. *The Annals of Statistics* 6, 461–464.
795 doi:10.1214/aos/1176344136.
- 796 Setsompop, K., Gagoski, B.A., Polimeni, J.R., Witzel, T., Wedeen, V.J., Wald, L.L., 2011. Blipped-
797 controlled aliasing in parallel imaging for simultaneous multislice echo planar imaging with re-
798 duced g -factor penalty. *Magnetic Resonance in Medicine* 67, 1210–1224. doi:10.1002/mrm.23097.
- 799 Shmueli, K., van Gelderen, P., de Zwart, J.A., Horovitz, S.G., Fukunaga, M., Jansma, J.M., Duyn,
800 J.H., 2007. Low-frequency fluctuations in the cardiac rate as a source of variance in the resting-
801 state fMRI BOLD signal. *NeuroImage* 38, 306–320. doi:10.1016/j.neuroimage.2007.07.037.

- 802 Sporns, O., Faskowitz, J., Teixeira, A.S., Cutts, S.A., Betzel, R.F., 2021. Dynamic expression of
803 brain functional systems disclosed by fine-scale analysis of edge time series. Network neuroscience
804 (Cambridge, Mass.) 5, 405–433. doi:10.1162/netn_a_00182.
- 805 Sreenivasan, K.R., Havlicek, M., Deshpande, G., 2015. Nonparametric hemodynamic deconvolution
806 of fMRI using homomorphic filtering. IEEE Transactions on Medical Imaging 34, 1155–1163.
807 doi:10.1109/tmi.2014.2379914.
- 808 Tagliazucchi, E., Balenzuela, P., Fraiman, D., Chialvo, D.R., 2012. Criticality in large-scale brain
809 fmri dynamics unveiled by a novel point process analysis. Frontiers in physiology 3, 15. doi:10.
810 3389/fphys.2012.00015.
- 811 Tagliazucchi, E., Balenzuela, P., Fraiman, D., Montoya, P., Chialvo, D.R., 2011. Spontaneous bold
812 event triggered averages for estimating functional connectivity at resting state. Neuroscience
813 letters 488, 158–163. doi:10.1016/j.neulet.2010.11.020.
- 814 Tagliazucchi, E., Siniatchkin, M., Laufs, H., Chialvo, D.R., 2016. The voxel-wise functional con-
815 nectome can be efficiently derived from co-activations in a sparse spatio-temporal point-process.
816 Frontiers in neuroscience 10, 381. doi:10.3389/fnins.2016.00381.
- 817 Tan, F.M., Caballero-Gaudes, C., Mullinger, K.J., Cho, S.Y., Zhang, Y., Dryden, I.L., Francis,
818 S.T., Gowland, P.A., 2017. Decoding fMRI events in sensorimotor motor network using sparse
819 paradigm free mapping and activation likelihood estimates. Human Brain Mapping 38, 5778–
820 5794. doi:10.1002/hbm.23767.
- 821 Tarun, A., Wainstein-Andriano, D., Sterpenich, V., Bayer, L., Perogamvros, L., Solms, M., Ax-
822 macher, N., Schwartz, S., Ville, D.V.D., 2020. NREM sleep stages specifically alter dynamical
823 integration of large-scale brain networks. iScience 24, 101923. doi:10.1101/2020.07.08.193508.
- 824 Tarun, A., Wainstein-Andriano, D., Sterpenich, V., Bayer, L., Perogramvos, L., Solms, M., Ax-
825 macher, N., Schwartz, S., Van De Ville, D., 2021. NREM sleep stages specifically alter dynamical
826 integration of large-scale brain networks. iScience 24, 101923. doi:10.1016/j.isci.2020.101923.
- 827 Tibshirani, R., 1996. Regression shrinkage and selection via the lasso. Journal of the Royal Statistical
828 Society: Series B (Methodological) 58, 267–288. doi:10.1111/j.2517-6161.1996.tb02080.x.
- 829 Triantafyllou, C., Hoge, R., Krueger, G., Wiggins, C., Potthast, A., Wiggins, G., Wald, L., 2005.
830 Comparison of physiological noise at 1.5 t, 3 t and 7 t and optimization of fMRI acquisition
831 parameters. NeuroImage 26, 243–250. doi:10.1016/j.neuroimage.2005.01.007.
- 832 Uruñuela, E., Jones, S., Crawford, A., Shin, W., Oh, S., Lowe, M., Caballero-Gaudes, C., 2020.
833 Stability-based sparse paradigm free mapping algorithm for deconvolution of functional MRI
834 data. Proceedings of the Annual International Conference of the IEEE Engineering in Medicine
835 and Biology Society, EMBS 2020-July, 1092–1095. doi:10.1109/embc44109.2020.9176137.
- 836 Uruñuela, E., Moia, S., Caballero-Gaudes, C., 2021. A low rank and sparse paradigm free mapping
837 algorithm for deconvolution of fMRI data doi:10.1109/isbi48211.2021.9433821.
- 838 Uruñuela-Tremiño, E., Moia, S., Gonzalez-Castillo, J., Caballero-Gaudes, C., 2019. Deconvolution
839 of multi-echo functional MRI data with multivariate multi-echo sparse paradigm free mapping.
840 ISMRM 27th Annual Meeting and Exhibition .

- 841 Yeşilyurt, B., Uğurbil, K., Uludağ, K., 2008. Dynamics and nonlinearities of the bold response at
842 very short stimulus durations. Magnetic resonance imaging 26, 853–862. doi:10.1016/j.mri.
843 2008.01.008.
- 844 Zhang, X., Pan, W.J., Keilholz, S.D., 2020. The relationship between BOLD and neural activity
845 arises from temporally sparse events. NeuroImage 207, 116390. doi:10.1016/j.neuroimage.
846 2019.116390.
- 847 Zoeller, D., Sandini, C., Karahanoglu, F.I., Schaer, M., Eliez, S., Van De Ville, D., 2019. Large-
848 scale brain network dynamics provide a measure of psychosis and anxiety in 22q11.2 deletion
849 syndrome. Biological Psychiatry: Cognitive Neuroscience and Neuroimaging 4, 881–892. doi:10.
850 1016/j.bpsc.2019.04.004.
- 851 Zöller, D., Sandini, C., Karahanoğlu, F.I., Padula, M.C., Schaer, M., Eliez, S., Ville, D.V.D.,
852 2019. Large-scale brain network dynamics provide a measure of psychosis and anxiety in 22q11.2
853 deletion syndrome. Biological Psychiatry: Cognitive Neuroscience and Neuroimaging 4, 881–892.
854 doi:10.1101/551796.

855 **Supplementary Material for Hemodynamic Deconvolution Demystified:**
856 **Sparsity-Driven Regularization at Work**

A



B

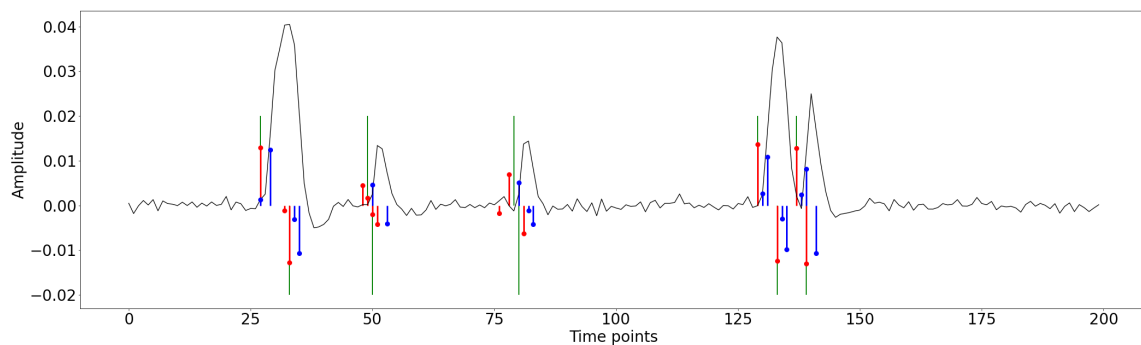


Figure S1: Activity-inducing (A) and innovation (B) signals estimated with PFM (red) and TA (blue) using their built-in HRF as opposed to using the same. The black line depicts the simulated signal, while the green lines indicate the onsets of the simulated neuronal events. X axis shows time in TRs.

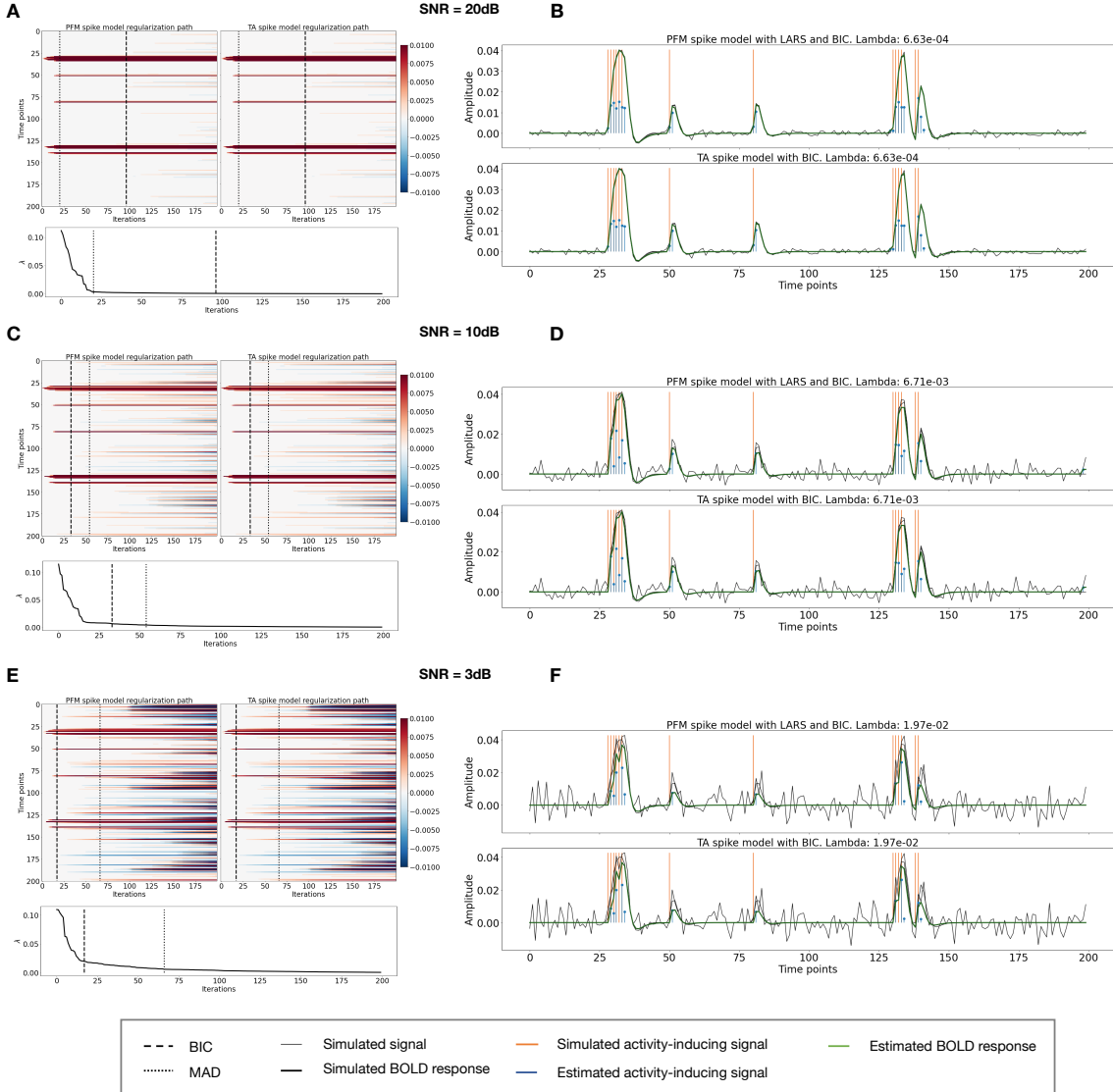


Figure S2: Spike model simulations. (Left) Heatmap of the regularization paths of the activity-inducing signal estimated with PFM and TA as a function of λ (increasing number of iterations in x-axis), whereas each row in the y-axis shows one time-point. Vertical lines denote iterations corresponding to the Akaike and Bayesian Information Criteria (AIC and BIC) optima. (Right) Estimated activity-inducing (blue) and activity-related (green) signals when set based on BIC. All estimates are identical, regardless of SNR.

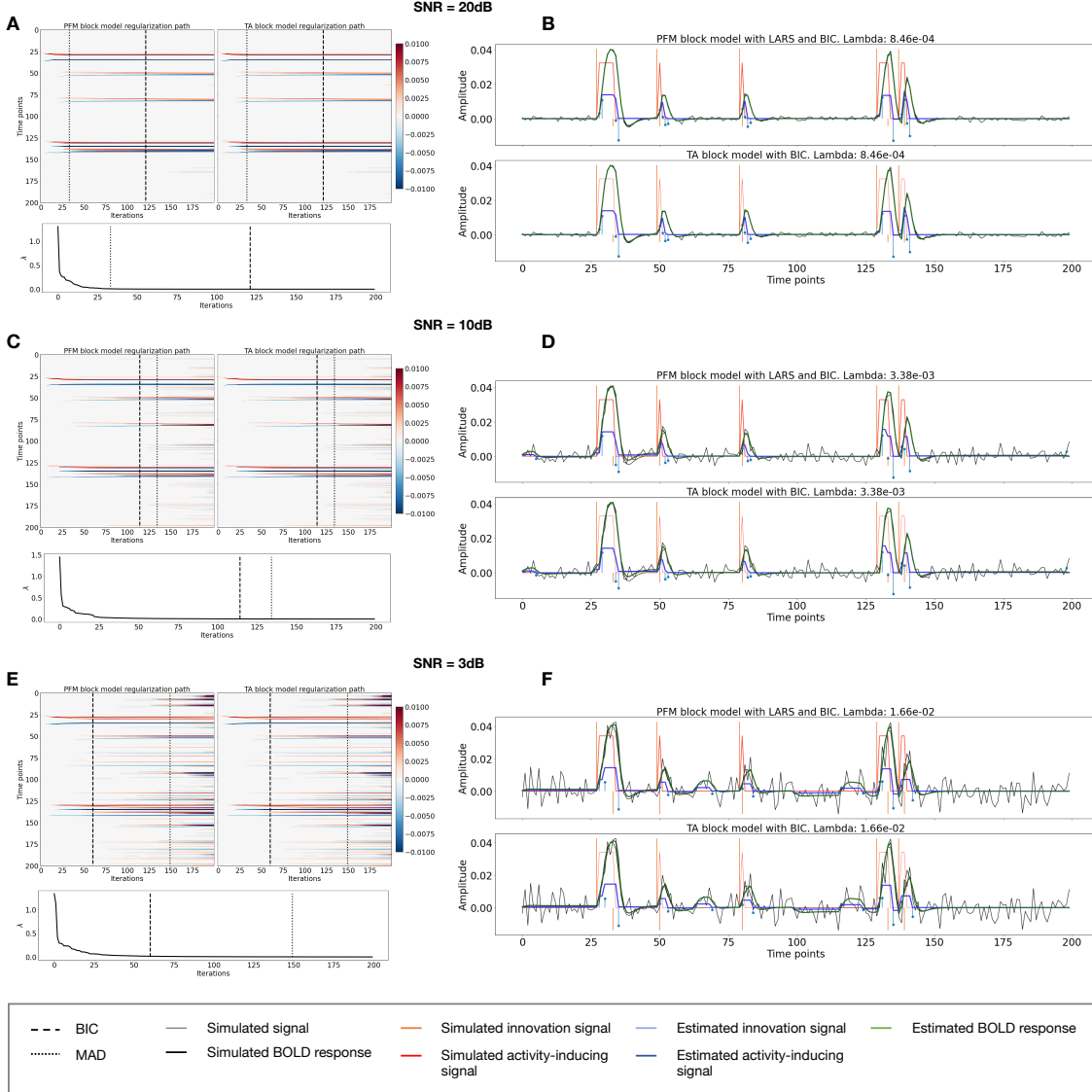


Figure S3: Block model simulations. (Left) Heatmap of the regularization paths of the innovation signal estimated with PFM and TA as a function of λ (increasing number of iterations in x-axis), whereas each row in the y-axis illustrates one time-point. Vertical lines denote iterations corresponding to the Akaike and Bayesian Information Criteria (AIC and BIC) optima. (Right) Estimated innovation (blue) and activity-related (green) signals when λ is set based on BIC. All the estimates are identical when compared between the PFM and TA cases, regardless of SNR.

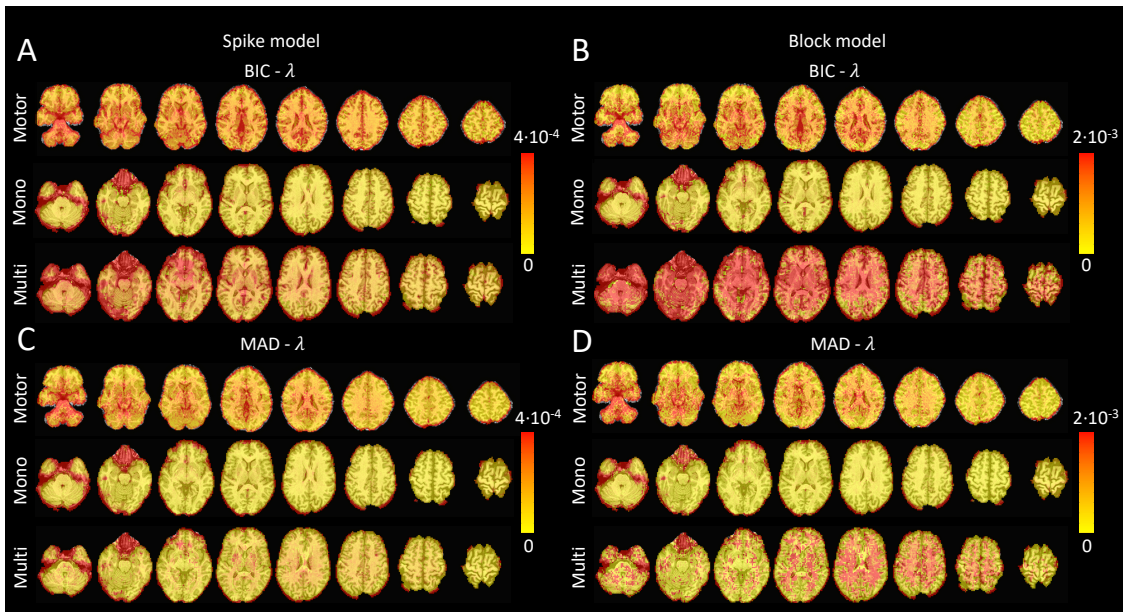


Figure S4: Values of λ across the different voxels in the brain used to estimate (A) the activity-inducing signal (spike model) and (B) the innovation signal (block model) with the BIC selection, as well as (C) the activity-inducing signal (block model) and (D) the innovation signal (block model) with a MAD-based selection. The λ maps are shown for the three experimental fMRI datasets: the motor task (Motor), the monoband resting-state (Mono), and the multiband resting-state (Multi) datasets.

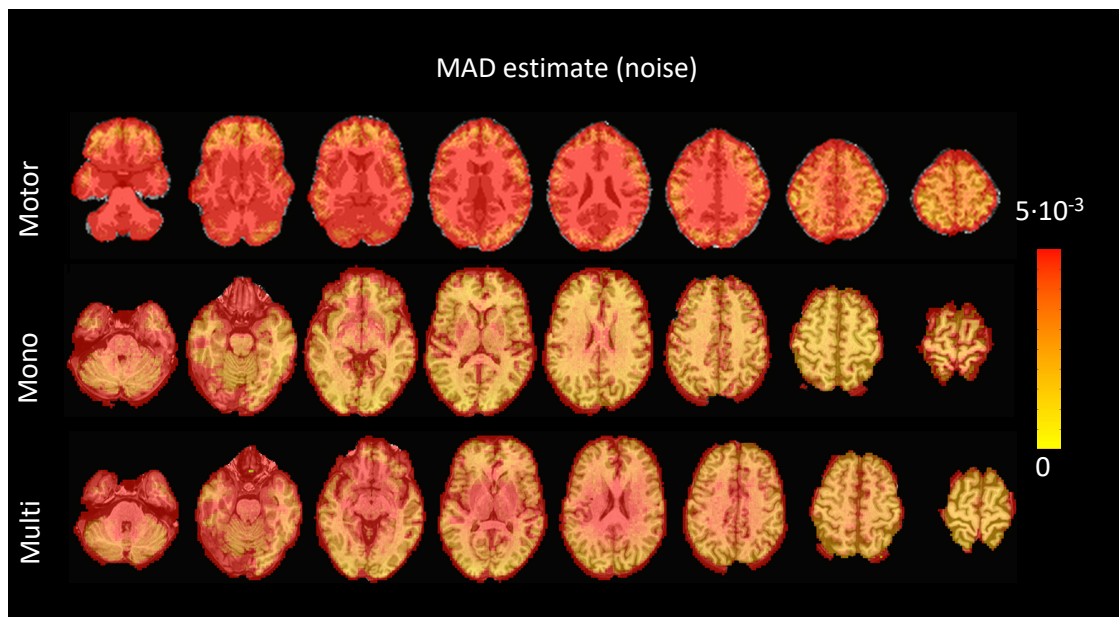


Figure S5: Values of the MAD estimate of standard deviation of the noise across the different voxels in the brain for the three experimental fMRI datasets: the motor task (Motor), the monoband resting-state (Mono), and the multiband resting-state (Multi) datasets.

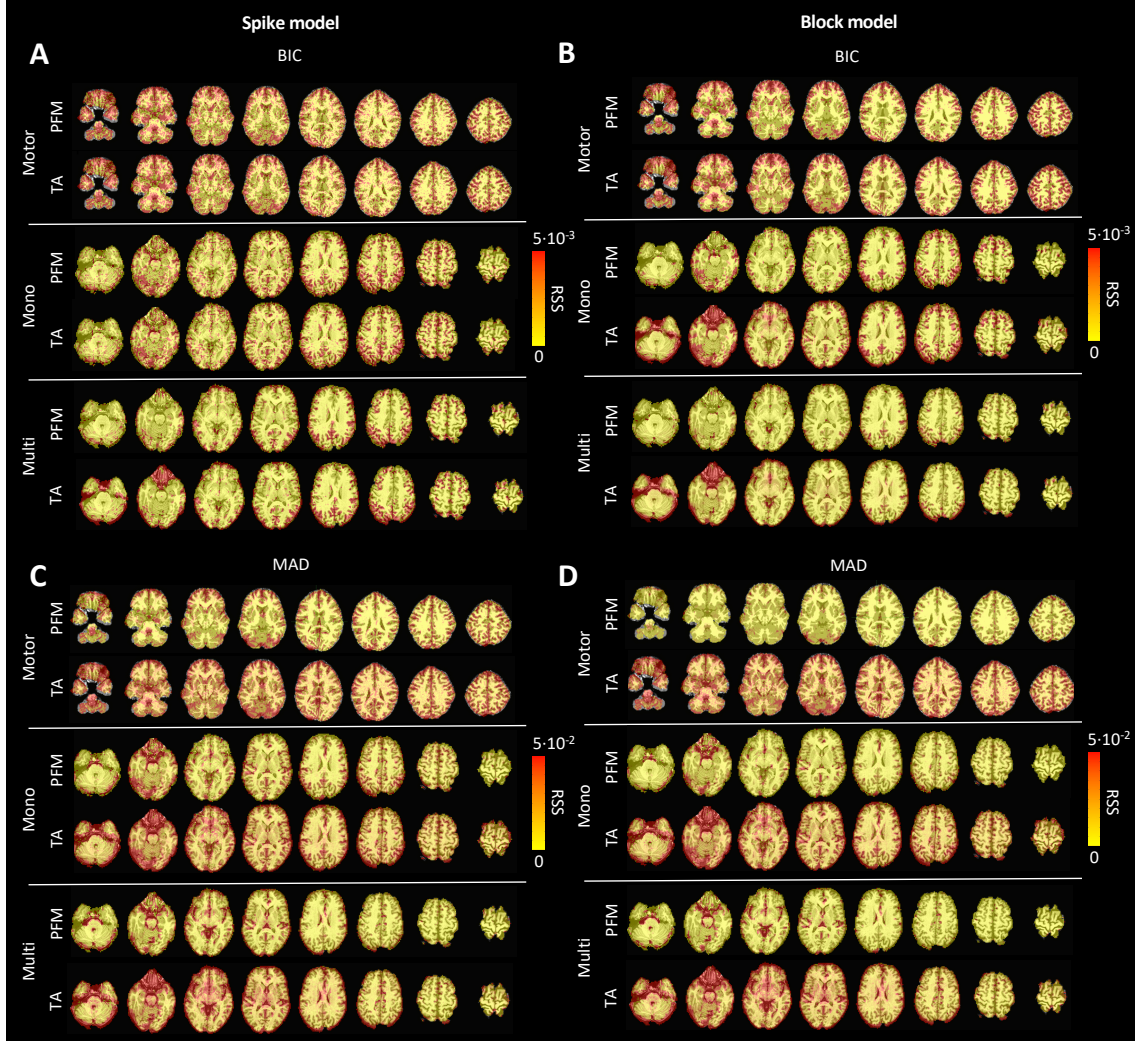


Figure S6: Root sum of squares (RSS) comparison between Paradigm Free Mapping and Total Activation for the three experimental fMRI datasets: the motor task (Motor), the monoband resting-state (Mono), and the multiband resting-state (Multi) datasets. RSS maps are shown for the spike (left) and block (right) models solved with a selection of λ based on the BIC (top) and MAD (bottom) criteria.

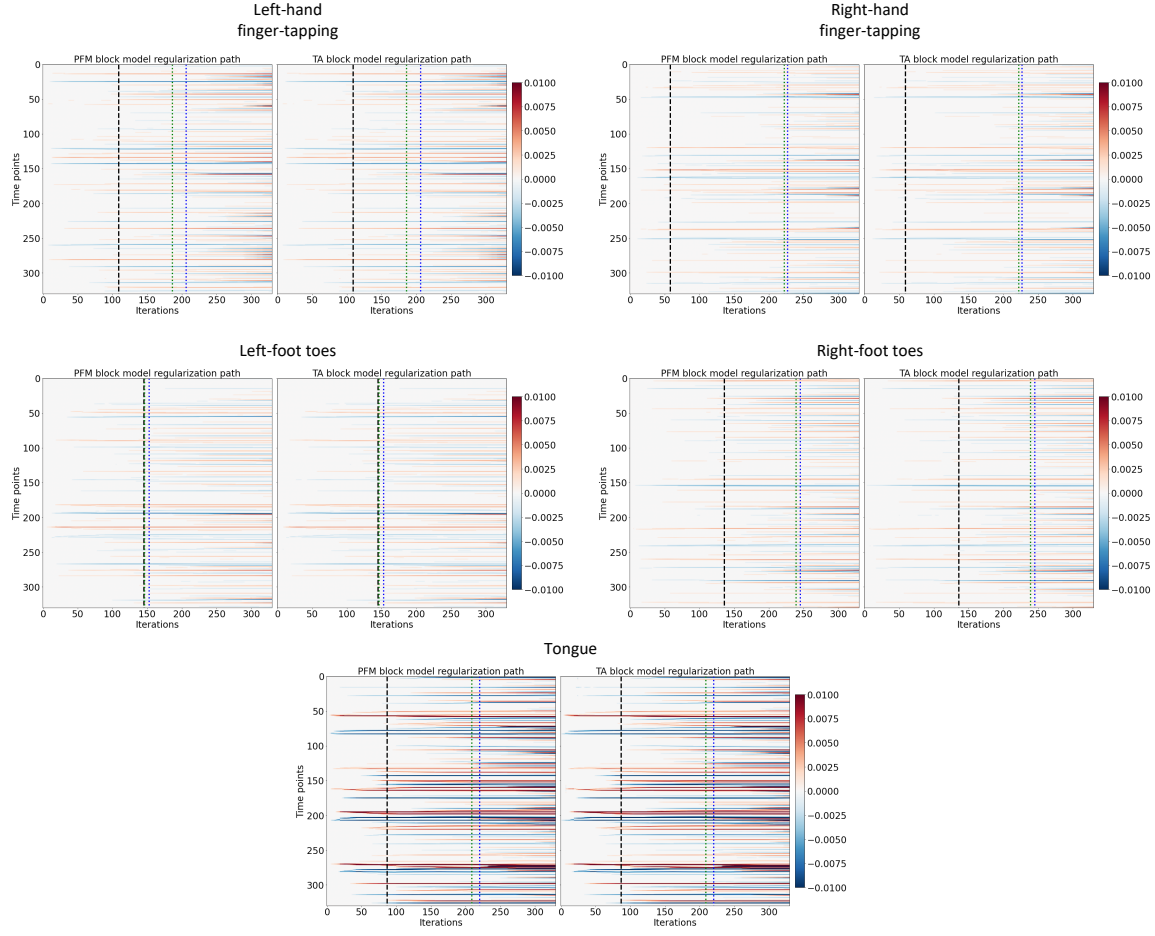


Figure S7: Regularization paths of the innovation signal estimated with PFM and TA as a function of λ (increasing number of iterations in x-axis, whereas each row in the y-axis shows one time-point) for the representative voxels of the motor task shown in Figure 5. Vertical lines denote selections of λ corresponding to the BIC (black), MAD based on LARS residuals (blue) and MAD based on FISTA residuals (green) optima.

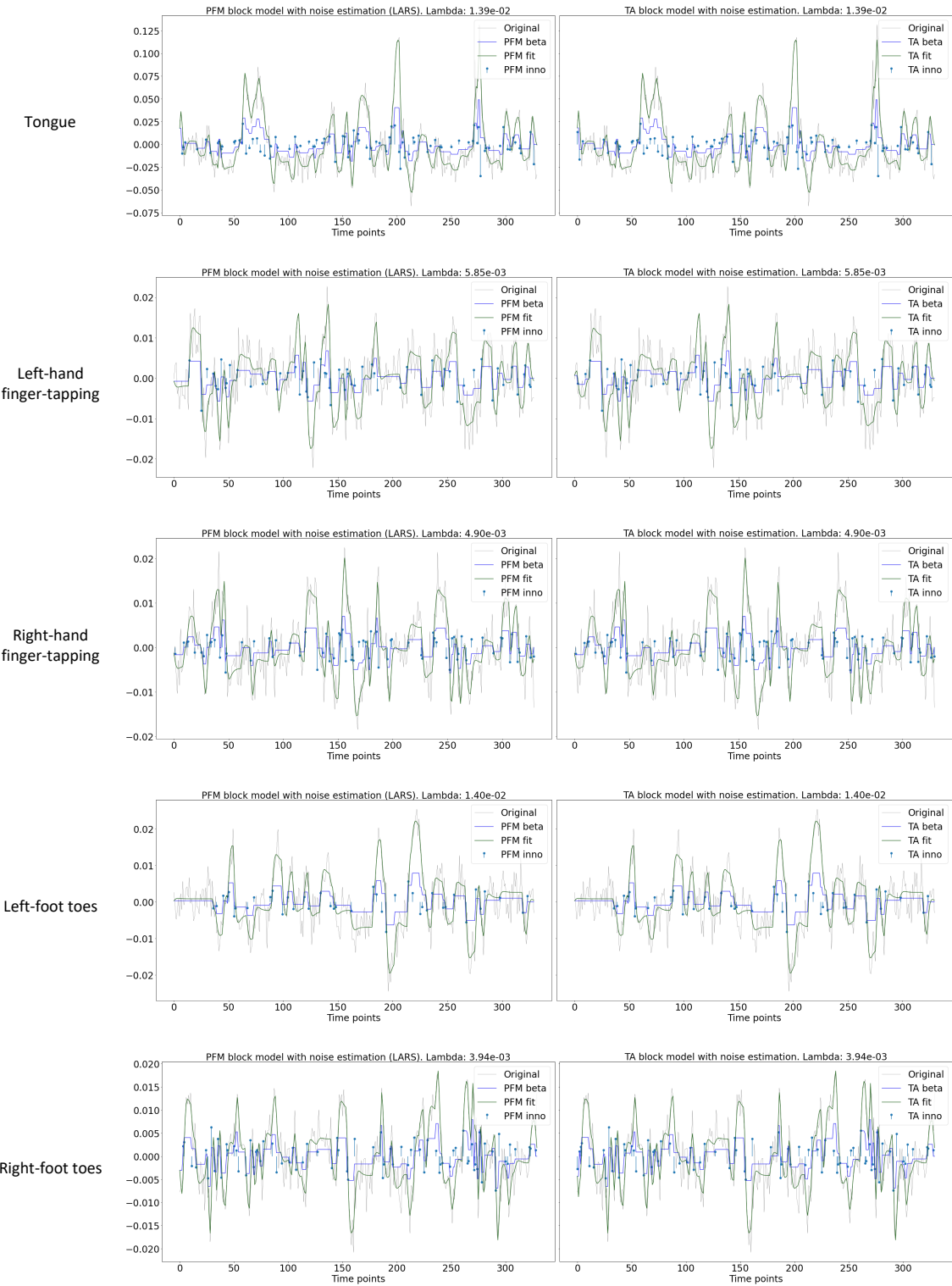


Figure S8: Estimated innovation signal (blue) and activity-related signal (green) for the representative voxels of the motor task shown in Figure 5 with the MAD selection of λ made by TA, i.e., employing the same λ with both PFM and TA.

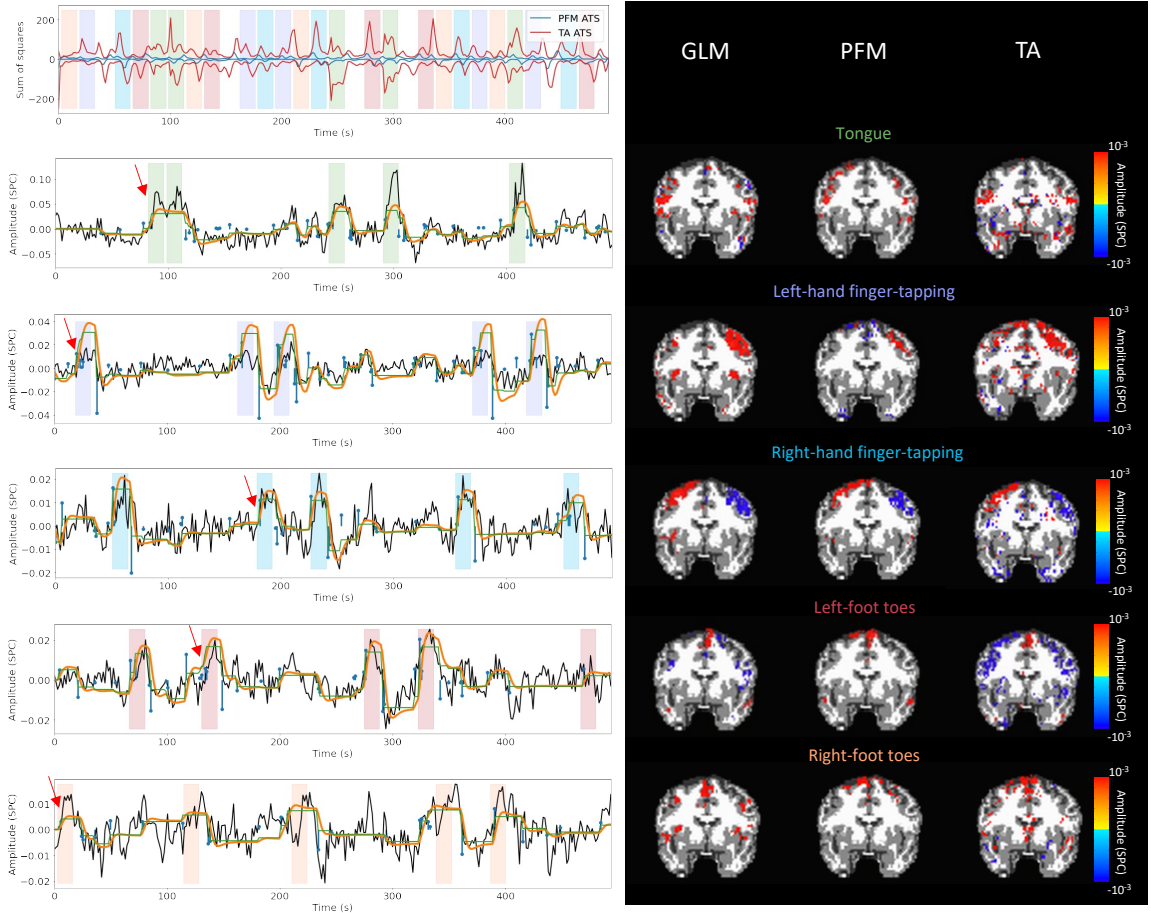


Figure S9: Activity maps of the motor task using a selection of λ based on the MAD estimate. Row 1: Activation time-series of the innovation signals estimated by PFM (in blue) or TA (in red) calculated as the sum of squares of all voxels at every timepoint. Positive-valued and negative-valued contributions were separated into two distinct time-courses. Color-bands indicate the onset and duration of each condition in the task (green: tongue, purple: left-hand finger-tapping, blue: right-hand finger-tapping, red: left-foot toes, orange: right-foot toes). Rows 2-6: time-series of a representative voxel for each task with the PFM-estimated innovation (blue), PFM-estimated activity-inducing (green), and activity-related (i.e., fitted, orange) signals, with their corresponding GLM, PFM, and TA maps on the right. The maps shown on the right are sampled at the time-point labeled with the red arrows and display the innovation signals at that moment across the whole brain.

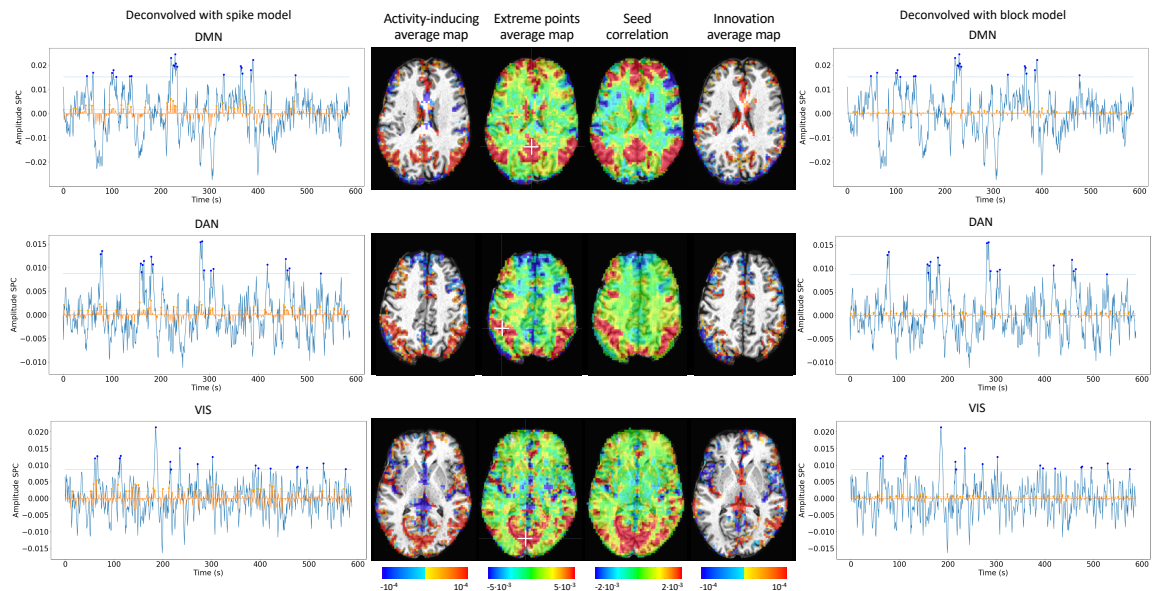


Figure S10: Activity-inducing CAPs (left) and innovation CAPs (right) obtained with the PFM-estimated activity-inducing and innovation signals respectively, using a MAD-based selection of λ . Time-points selected with a 95th percentile threshold are shown over the average time-series (blue) in the seed region (white-cross) and the deconvolved signal (orange). CAPs and seed correlation maps are illustrated in the center.